NONPRINCIPAL-PLANE SCATTERING FROM FLAT PLATES — SECOND-ORDER AND CORNER DIFFRACTION AND PATTERN CONTROL OF HORN ANTENNAS

Semiannual Progress Report

PART A

Constantine A. Balanis and Lesley A. Polka

February 1, 1989 - July 31, 1989

PART B

Constantine A. Balanis and Kefeng Liu

February 1, 1989 - July 31, 1989

Telecommunications Research Center
Department of Electrical and Computer Engineering
Arizona State University
Tempe, AZ 85287

Grant No. NAG-1-562
National Aeronautics and Space Administration
Langley Research Center
Hampton, VA 23665

ABSTRACT

Part A of this report examines several high-frequency models for nonprincipal-plane scattering from a rectangular, perfectly conducting plate. Two methods, the Method of Equivalent Currents and corner diffraction coefficients, are considered. Formulations for second-order Physical Theory of Diffraction equivalent currents and for corner diffracted fields are presented. Comparisons are made among the following plate models: first-order Physical Optics equivalent currents, first-order Geometrical Theory of Diffraction equivalent currents, first-order Physical Optics/Physical Theory of Diffraction equivalent currents, second-order Physical Theory of Diffraction equivalent currents, corner diffraction coefficients, Moment Method, and experimental results. Results away from grazing are accurate using only first-order terms. Near grazing, second-order and corner diffraction terms improve the results for many cases.

Part B of the report investigates the pattern control of horn antennas using lossy materials to coat the inner walls of the horn. Integral Equation and Moment Method techniques are used to formulate the problem. It is clearly demonstrated that side lobe level reduction can be achieved using impedance surfaces on the inner walls of the horn.

PART A

NONPRINCIPAL-PLANE SCATTERING FROM FLAT PLATES — SECOND-ORDER AND CORNER DIFFRACTIONS

PART A

NONPRINCIPAL-PLANE SCATTERING FROM FLAT PLATES — SECOND-ORDER AND CORNER DIFFRACTIONS

I. Introduction

The modeling of a perfectly-conducting, rectangular plate for scattering in nonprincipal planes using the Method of Equivalent (MEC) currents was discussed in a previous report [1]. Two models using only first-order equivalent currents were presented. The first model used Geometrical Theory of Diffraction (GTD) equivalent currents [2]-[3], which are well behaved for monostatic scattering but contain singularities for bistatic scattering. A second model using Physical Optics (PO) [4] and Physical Theory of Diffraction (PTD) [5] equivalent currents was developed. These currents are well behaved for both monostatic and bistatic RCS predictions. The GTD and PO/PTD equivalent currents models give similar results and compare favorably with moment method (MM) and experimental results away from regions near and at grazing incidence. Near and at grazing incidence, higher-order scattering and corner diffraction mechanisms were thought to be significant factors in the total scattered field and a means of including these components was desired.

In this report, two new models of the plate for nonprincipal-plane scattering are explored. The first is a revised version of the PO/PTD model with second-order PTD equivalent currents [6] included to account for second-order interactions among the plate edges. The second model uses a heuristically derived corner diffraction coefficient [7], [8] to account for the corner scattering mechanism. The patterns obtained using the newer models are comparedto the data of the previously reported models, MM, and experimental results.

II. Theory

A. Second-Order PTD Equivalent Currents

As with many versions of the MEC, the second-order PTD equivalent currents are formulated using the canonical perfectly conducting, infinite wedge geometry which is used to approximate other geometries. For the rectangular plate shown in Fig. 1, each edge is modeled as an infinite half-plane by setting the exterior wedge angle to 2π. This is a valid approximation as long as the edges are electrically isolated; thus, the accuracy of this model increases as the electrical size of the plate increases. The general wedge geometry is shown in Fig. 2. This geometry is applicable to both first- and second-order equivalent currents. The directional vectors and angles are:

$\hat{s}'$ = the unit vector in the direction of incidence.

$\hat{s}$ = the unit vector in the direction of observation.

$\hat{t}$ = the unit vector tangent to the edge of interest, directed so that it encircles the scatterer in a counterclockwise manner.

$\hat{n}$ = the unit vector normal to the edge of interest, lying on the illuminated face.

β_o' = the angle between $\hat{s}'$ and the edge.

β_o = the angle between $\hat{s}$ and the edge.

ψ' = the angle between the illuminated face and the edge-fixed plane of incidence.

ψ = the angle between the illuminated face and the edge-fixed plane of observation.

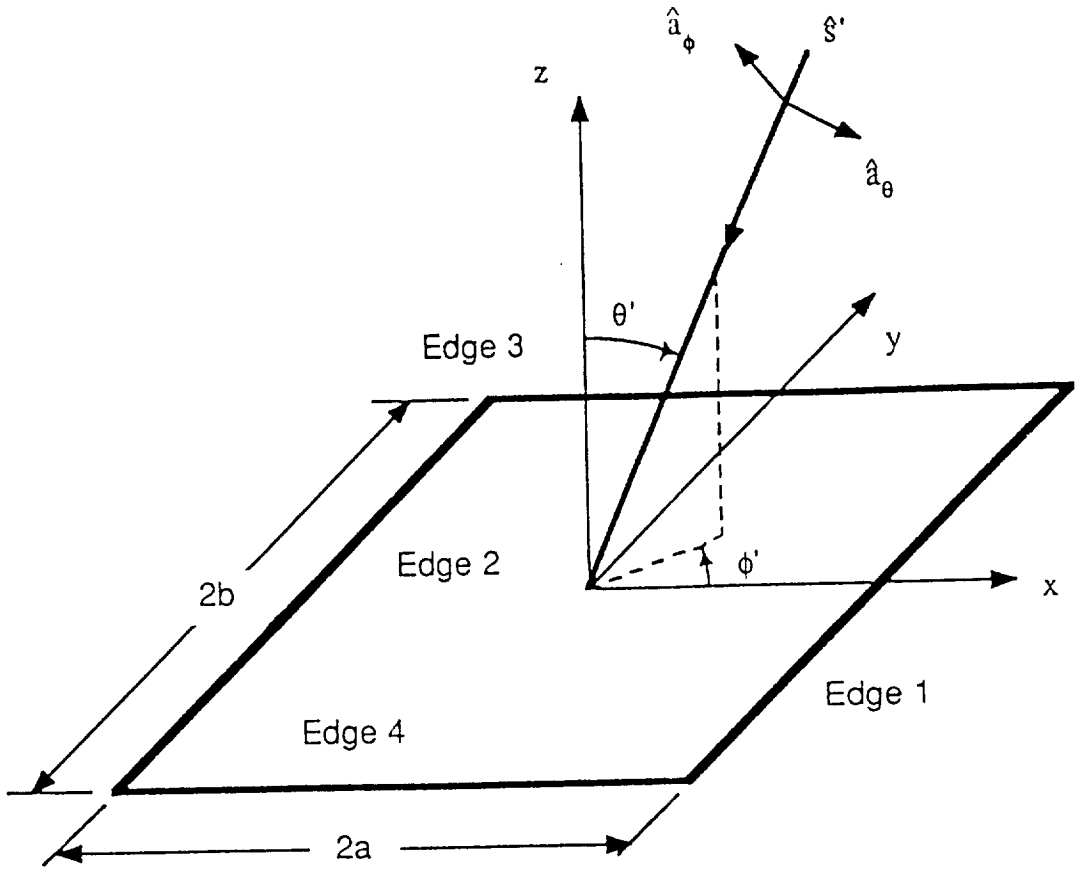

Fig. 1. Plate geometry.

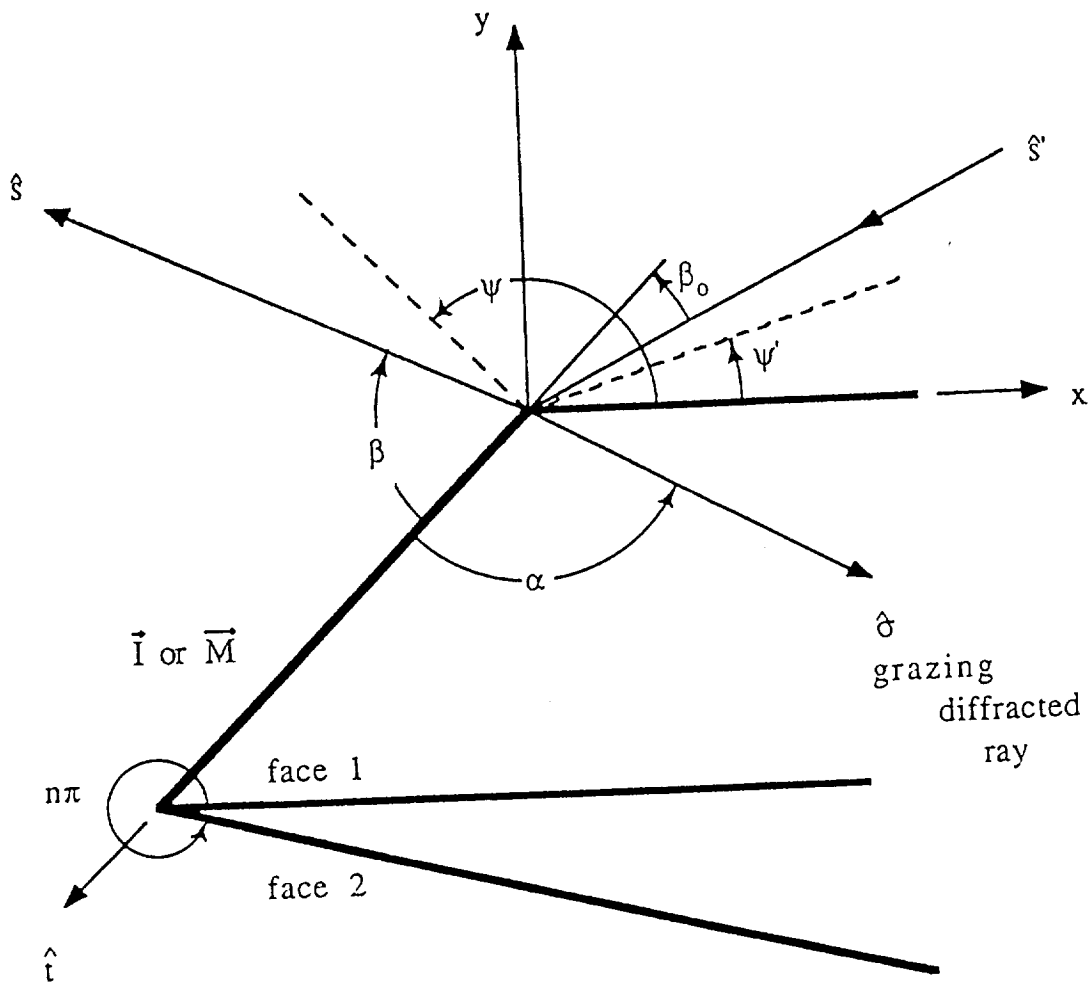

Fig. 2. Wedge geometry for equivalent currents derivation.

α = the skew angle of integration across the surface.

In terms of the directional vectors, the directional angles are:

$$\beta_o' = \cos^{-1}(\hat{s}' \cdot \hat{t}) \tag{1a}$$

$$\beta_o = \cos^{-1}(\hat{s} \cdot \hat{t}) \tag{1b}$$

$$\psi' = \cos^{-1}\left\{\left[\frac{\hat{s}' \times \hat{t}}{|\hat{s}' \times \hat{t}|} \times \hat{t}\right] \cdot \hat{n}\right\} \tag{1c}$$

$$\psi = \cos^{-1}\left\{\left[\frac{\hat{s} \times \hat{t}}{|\hat{s} \times \hat{t}|} \times \hat{t}\right] \cdot \hat{n}\right\} \tag{1d}$$

For monostatic scattering, $\psi = \psi'$, $\beta_o = \pi - \beta_o'$, and $\hat{s} = -\hat{s}'$. For the flat plate, the unit vector in the direction of incidence for the geometry considered is:

$$\hat{s}' = -\hat{a}_r = -\hat{a}_x \sin\theta'\cos\phi' - \hat{a}_y \sin\theta'\sin\phi' - \hat{a}_z \cos\theta' \tag{2}$$

A different set of directional vectors and angles must be formulated for each edge. The vectors for each edge are:

Edge 1: $\hat{t}_1 = \hat{a}_y$ $\qquad$ $\hat{n}_1 = -\hat{a}_x$ (3a)

Edge 2: $\hat{t}_2 = -\hat{a}_y$ $\qquad$ $\hat{n}_2 = \hat{a}_x$ (3b)

Edge 3: $\hat{t}_3 = -\hat{a}_x$ $\qquad$ $\hat{n}_3 = -\hat{a}_y$ (3c)

Edge 4: $\hat{t}_4 = \hat{a}_x$ $\qquad$ $\hat{n}_4 = \hat{a}_y$ (3d)

The resulting β_o' functions for each edge are:

Edge 1: $\cos\beta_{o_1}' = -\sin\theta'\sin\phi'$ (4a)

$$\sin\beta_{o_1}' = \sqrt{1 - \sin^2\theta'\sin^2\phi'} \tag{4b}$$

Edge 2: $\cos\beta_{o_2}' = -\cos\beta_{o_1}'$ (4c)

$$\sin\beta_{o_2}' = \sin\beta_{o_1}' \tag{4d}$$

Edge 3: $\cos\beta_{o_3}' = \sin\theta'\cos\phi'$ (4e)

$$\sin\beta_{o_3}' = \sqrt{1 - \sin^2\theta'\cos^2\phi'} \quad (4f)$$

Edge 4: $\cos\beta_{o_4}' = -\cos\beta_{o_3}'$ (4g)

$$\sin\beta_{o_4}' = \sin\beta_{o_3}' \quad (4h)$$

Using the β_o' definitions, the ψ' functions can be expressed as:

Edge 1: $$\cos\psi_1 = \frac{-\sin\theta'\cos\phi'}{\sin\beta_{o_1}'} \quad (5a)$$

$$\sin\psi_1 = \frac{\cos\theta'}{\sin\beta_{o_1}'} \quad (5b)$$

Edge 2: $\cos\psi_2 = -\cos\psi_1$ (5c)

$$\sin\psi_2 = \sin\psi_1 \quad (5d)$$

Edge 3: $$\cos\psi_3 = \frac{-\sin\theta'\sin\phi'}{\sin\beta_{o_3}'} \quad (5e)$$

$$\sin\psi_3 = \frac{\cos\theta'}{\sin\beta_{o_3}'} \quad (5f)$$

Edge 4: $\cos\psi_4 = -\cos\psi_3$ (5g)

$$\sin\psi_4 = \sin\psi_3 \quad (5h)$$

For each edge the tangential components of the incident electric and magnetic fields are needed to determine the corresponding equivalent currents. Both soft and hard polarizations are considered. The incident fields are:

Soft Polarization

$$\underline{E}^i = \hat{a}_\phi \, E_o \, e^{-j\underline{k}\cdot\underline{r}} \quad (6a)$$

$$\underline{H}^i = \hat{a}_\theta \, (1/\eta) \, E_o \, e^{-j\underline{k}\cdot\underline{r}} \quad (6b)$$

Hard Polarization

$$\underline{E}^i = \hat{a}_\theta \, E_o \, e^{-j\underline{k}\cdot\underline{r}} \tag{6c}$$

$$\underline{H}^i = -\hat{a}_\phi \, (1/\eta) \, E_o \, e^{-j\underline{k}\cdot\underline{r}} \tag{6d}$$

To simplify the rectangular plate analysis, the incident fields are transformed to the rectangular coordinate system. The position vector, $\underline{r}$, is:

$$\underline{r} = \hat{a}_x \, x + \hat{a}_y \, y + \hat{a}_z \, z \tag{7}$$

The propagation vector, $\underline{k}$, for the incident field is:

$$\underline{k} = -k \, \hat{a}_r = -k(\hat{a}_x \sin\theta'\cos\phi' + \hat{a}_y \sin\theta'\sin\phi' + \hat{a}_z \cos\theta') \tag{8}$$

With respect to the rectangular coordinate system, the incident fields are:

Soft Polarization

$$\underline{E}^i = E_o \, e^{jk(x\sin\theta'\cos\phi' + y\sin\theta'\sin\phi' + z\cos\theta')} \times [-\hat{a}_x \sin\phi' + \hat{a}_y \cos\phi'] \tag{9a}$$

$$\underline{H}^i = (1/\eta) \, E_o \, e^{jk(x\sin\theta'\cos\phi' + y\sin\theta'\sin\phi' + z\cos\theta')} \times [\hat{a}_x \cos\theta'\cos\phi' + \hat{a}_y \cos\theta'\sin\phi' + \hat{a}_z \sin\theta'] \tag{9b}$$

Hard Polarization

$$\underline{E}_i = E_o \, e^{jk(x\sin\theta'\cos\phi' + y\sin\theta'\sin\phi' + z\cos\theta')} \times [\hat{a}_x \cos\theta'\cos\phi' + \hat{a}_y \cos\theta'\sin\phi' + \hat{a}_z \sin\theta'] \tag{9c}$$

$$\underline{H}_i = -(1/\eta) \, E_o \, e^{jk(x\sin\theta'\cos\phi' + y\sin\theta'\sin\phi' + z\cos\theta')} \times [-\hat{a}_x \sin\phi' + \hat{a}_y \cos\phi'] \tag{9d}$$

The scattered fields for far-field observations are expressed in terms of the vector potentials:

$$E_r \cong 0 \tag{10a}$$

$$E_\theta \cong -j\omega \left[A_\theta + \eta F_\phi\right] \tag{10b}$$

$$E_\phi \cong -j\omega \left[A_\phi - \eta F_\theta\right] \tag{10c}$$

The vector potentials are:

$$\underline{A} = \frac{\mu}{4\pi} \int_C \underline{I}(x',y',z') \frac{e^{-jkr}}{R} d\ell' \tag{11a}$$

$$\underline{F} = \frac{\varepsilon}{4\pi} \int_C \underline{M}(x',y',z') \frac{e^{-jkr}}{R} d\ell' \tag{11b}$$

For far-field analysis, the following simplifications can be made:

$$R \cong r - r'\cos\vartheta = r - \underline{r}' \cdot \hat{a}_r \quad \text{(for phase variation)} \tag{12a}$$

$$R \cong r \quad \text{(for amplitude variation)} \tag{12b}$$

where

$$\underline{r}' = \hat{a}_x\, x + \hat{a}_y\, y \tag{13}$$

for the flat plate oriented as in Fig. 1. For phase variation:

$$R \cong r - x\sin\theta'\cos\phi' - y\sin\theta'\sin\phi' \tag{14}$$

Finally, the vector potentials for far-field scattering from the plate become:

$$\underline{A} = \frac{\mu}{4\pi} \frac{e^{-jkr}}{r} \int_C \underline{I}(x,y,z)\, e^{jk(x\sin\theta'\cos\phi' + y\sin\theta'\sin\phi')}\, d\ell \tag{15a}$$

$$\underline{F} = \frac{\varepsilon}{4\pi} \frac{e^{-jkr}}{r} \int_C \underline{M}(x,y,z)\, e^{jk(x\sin\theta'\cos\phi' + y\sin\theta'\sin\phi')}\, d\ell \tag{15b}$$

The integrals are evaluated along the perimeter of the plate in a counterclockwise manner. On the surface of the plate, z=0. Also, for each edge, the coordinates are:

$$\text{Edge 1:} \quad x = a \qquad -b \le y \le b \tag{16a}$$

$$\text{Edge 2:} \quad x = -a \qquad -b \le y \le b \tag{16b}$$

$$\text{Edge 3:} \quad -a \le x \le a \qquad y = b \tag{16c}$$

$$\text{Edge 4:} \quad -a \le x \le a \qquad y = -b \tag{16d}$$

To simplify the derivation, each vector potential integral is represented as a sum of four integrals, each corresponding to an edge of the plate. For the second-order currents, numerical integration is used in evaluating the integrals. $\underline{I}$ and $\underline{M}$ must be determined separately for each edge taking into account the individual geometries. Again, each edge is viewed as the truncation of an infinite half-plane.

The general geometry for the formulation of the second-order currents is shown in Fig. 3. The directional vectors and angles are for the edge of first-order diffraction defined above in the description of Fig. 2. The diffracted ray travels along $\hat{\sigma}$ at a skew angle of β_o'. The axis of integration across the structure is again $\hat{\sigma}$, which effectively eliminates all singularities except the Ufimtsev singularity for forward observation at grazing incidence. The distance from the first point of diffraction, O_1, to the second point, O_2, is ℓ. The tangent vectors to the edge of first diffraction is $\hat{t}_1$

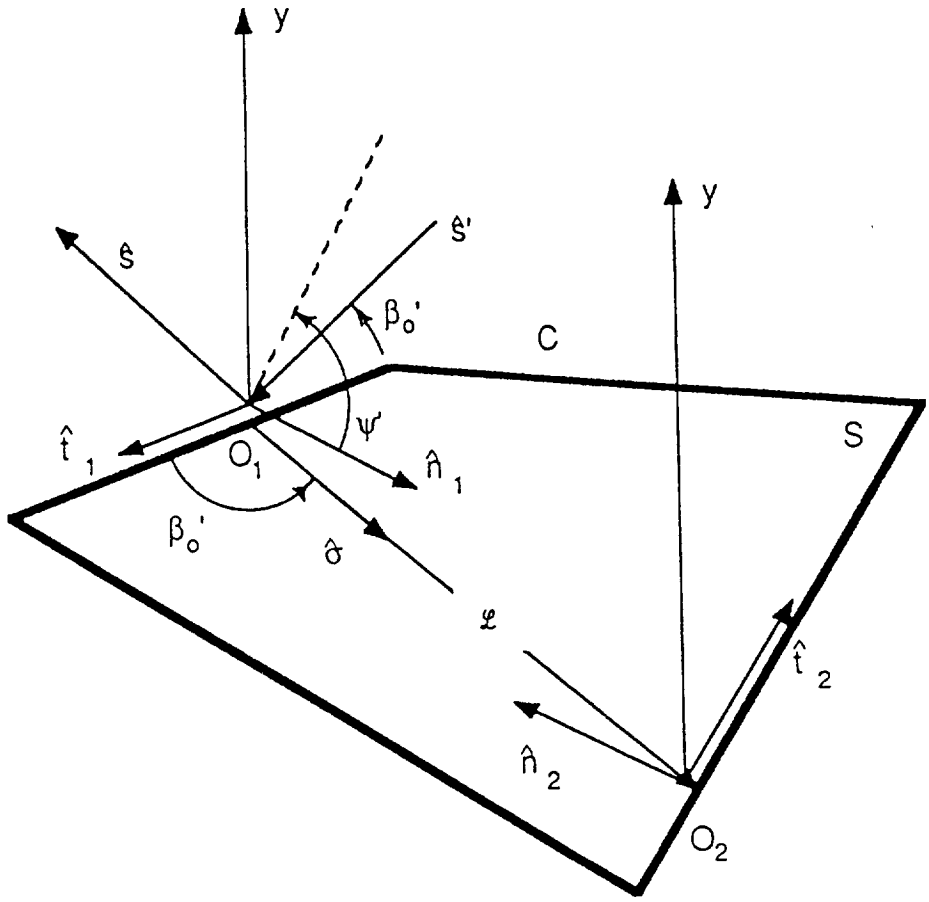

Fig. 3. Geometry for second-order components.

and the vector at the second edge is $\hat{t}_2$. These are oriented so that they encircle the scatterer in a counterclockwise manner.

The second-order PTD equivalent currents components are defined as:

$$M_2^f = \frac{\eta}{\sin^2\beta_2} \; \hat{t}_2 \cdot [\, \hat{s} \times \underline{K}_2^f \,] \tag{17a}$$

$$I_1^f = \frac{1}{\sin^2\beta_2} \; \hat{s} \cdot [(\hat{t}_2 \times \hat{s}) \cdot \underline{K}_2^f \,] \tag{17b}$$

where

$$\underline{K}_2^f = |\hat{\sigma} \times \hat{t}_2| \; e^{-jk\mathcal{L}\,(\hat{\sigma}\,\cdot\,\hat{s})} \int \bar{j}^f \, e^{jk\sigma\,(\hat{\sigma}\,\cdot\,\hat{s})} \, d\sigma \tag{17c}$$

The surface fringe current density, $\bar{j}^f$, is expressed in terms of the exact fringe-current scattering solution to the wedge; therefore, $\underline{K}_2^f$ consists of a contour integral in the complex plane that is integrated along $\hat{\sigma}$ and evaluated only at the upper endpoint. $\underline{K}_2^f$ is evaluated using the Method of Steepest Descent and the result for a half-plane is [5]:

$$\underline{K}_2^f = \frac{4\sqrt{2}\;|\hat{\sigma} \times t_2|\; e^{-jk\mathcal{L}}}{jk\sin^2\beta_o'\,(\mu+\cos\psi')} \left\{ \frac{F\,[\sqrt{L(1-\mu)}\,]}{\sqrt{1-\mu}} \times \right.$$

$$[\hat{n}_1(\hat{t}_1 \cdot \underline{H}_o^i)\cos(\psi'/2) + \hat{t}_1(\hat{t}_1 \cdot \underline{H}_o^i)\mu\cot\beta_o'\cos(\psi'/2)$$

$$+ \hat{t}_1(\hat{t}_1 \cdot \underline{E}_o^i)\,(1/\eta)\,(1-\mu)\csc\beta_o'\sin(\psi'/2)\,]$$

$$- \frac{F\,[\sqrt{L(1+\cos\psi')}\,]}{\sqrt{2}}\,[\hat{n}_1(\hat{t}_1 \cdot \underline{H}_o^i) - \hat{t}_1\,(\hat{t}_1 \cdot \underline{H}_o^i)\cot\beta_o'\cos\psi'$$

$$+ \hat{t}_1(\hat{t}_1 \cdot \underline{E}_o^i)\,(1/\eta)\csc\beta_o' \sin\psi']\Big\} \tag{18}$$

The expressions for the currents simplify to:

$$M_2^f = -\eta\, \hat{n}_2 \cdot \underline{K}_2^f \frac{\sin\psi_2}{\sin\beta_2} \tag{19a}$$

$$I_2^f = \hat{t}_2 \cdot \underline{K}_2^f - \hat{n}_2 \cdot \underline{K}_2^f \cot\beta_2 \cos\psi_2 \tag{19b}$$

where $\underline{K}_2^f$ is given in (18) for a half-plane. Other necessary quantities are:

$\hat{t}_1$, $\hat{t}_2$ = the unit vectors tangent to the edges of first- and second-order diffractions, respectively, oriented so that they encircle the scatterer in a counterclockwise manner.

$\hat{n}_1$, $\hat{n}_2$ = the unit vectors normal to the edges of first- and second-order diffractions, respectively, pointing inward and lying on the illuminated surface of the scatterer.

$\hat{\sigma}$ = the unit vector in the direction of integration skewed at an angle β_o' with respect to the edge of the wedge so that it represents the grazing diffracted ray.

or

$$\hat{\sigma} = \hat{n}_1 \sin\beta_o' + \hat{t}_1 \cos\beta_o' \tag{20a}$$

ℓ = the distance along $\hat{\sigma}$ from O_1 to O_2, the points of first- and second-order diffraction, respectively.

$$L = k\ell \sin^2\beta_o' \tag{20b}$$

$F(x)$ = the modified Fresnel transition function.

or
$$F(x) = \sqrt{j/\pi}\, e^{jx^2} \int_x^\infty e^{-jt^2} dt \tag{20c}$$

$$\mu = \frac{\cos\gamma - \cos^2\beta_o'}{\sin^2\beta_o'} = 1 - 2\,\frac{\sin^2(\gamma/2)}{\sin^2\beta_o'} \qquad (20d)$$

γ = the angle between $\hat{\sigma}$ and $\hat{s}$.

$$\cos\gamma = \hat{\sigma} \cdot \hat{s} = \sin\beta_o'\sin\beta_1\cos\psi_1 + \cos\beta_o'\cos\beta_1 \qquad (20e)$$

ψ_i, β_i = the polar angles of $\hat{s}$ in the coordinate system local to the edge of interest, the n_i, y, t_i coordinate system.

where

$$\cos\beta_i = \hat{s} \cdot \hat{t}_i \qquad (20f)$$

$$\sin\beta_i\cos\psi_i = \hat{s} \cdot \hat{n}_i \qquad (20g)$$

$$\sin\beta_i\sin\psi_i = \hat{s} \cdot \hat{y} \qquad (20h)$$

The directional angles β_o', β_o, ψ', and ψ are defined in (4) and (5).

The second-order diffracted field is obtained by substituting M_2^f and I_2^f from (19) into the vector potential integrals of (11), integrating, and then substituting into (10). Numerical integration must usually be used to find the integrals of (11). The limits of integration on the integrals of (11) are found using ray tracing. The area that the first-order fields affect is bounded by the two extreme first-order diffracted rays. Fig. 4 illustrates this procedure. Edge AB illuminates the curve from A′ to B′. Integration is along the boundary from A′ to B′. Often illuminated regions overlap due to interactions from many edges.

The total first- and second-order fields are found by adding the fields due to scattering by the PO currents, the PTD components, and

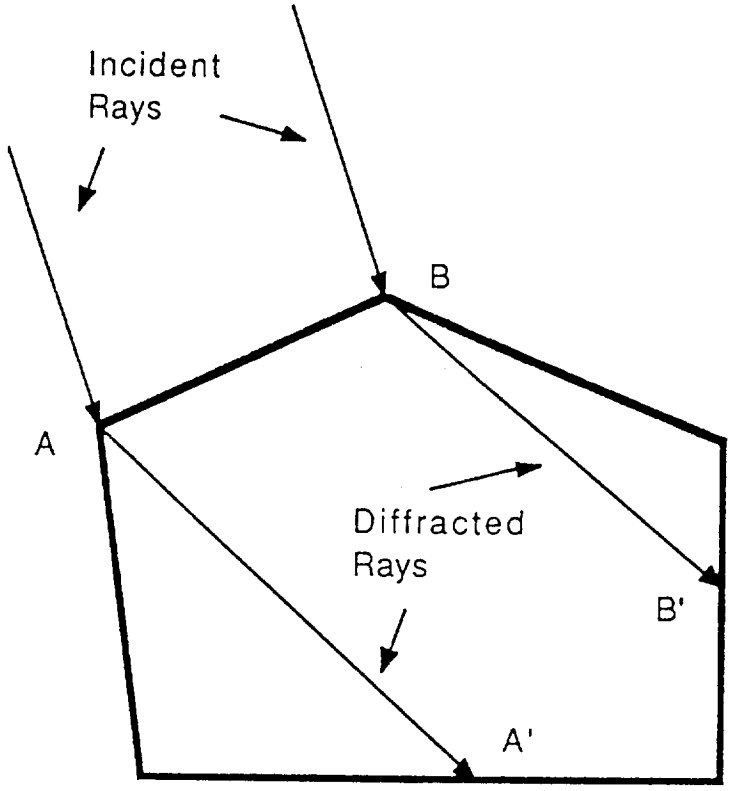

Fig. 4. Geometry for illumination of the second edge.

the second-order components. These fields are valid for all directions of illumination and observation, on and off the Keller cone of diffracted rays, except for the forward direction due to grazing incidence where an infinite singularity exists. This is the Ufimtsev singularity.

In terms of the directional vectors, the directional angles are:

$$\cos\beta_2 = \hat{s} \cdot \hat{t} \tag{21a}$$

$$\sin\beta_2\cos\psi_2 = \hat{s} \cdot \hat{n}_2 \tag{21b}$$

$$\sin\beta_2\sin\psi_2 = \hat{s} \cdot \hat{y} \tag{21c}$$

For each edge of second-order diffraction, the directional vectors are:

$$\text{Edge 1:} \quad \hat{t}_{21} = \hat{a}_y \qquad \hat{n}_{21} = -\hat{a}_x \tag{22a}$$

$$\text{Edge 2:} \quad \hat{t}_{22} = -\hat{a}_y \qquad \hat{n}_{22} = \hat{a}_x \tag{22b}$$

$$\text{Edge 3:} \quad \hat{t}_{23} = -\hat{a}_x \qquad \hat{n}_{23} = -\hat{a}_y \tag{22c}$$

$$\text{Edge 4:} \quad \hat{t}_{24} = \hat{a}_x \qquad \hat{n}_{24} = \hat{a}_y \tag{22d}$$

Using the definitions of (22) in the equations of (21) along with the definition of $\hat{s}'$ from (2), the factors $\frac{\sin\psi_2}{\sin\beta_2}$ and $\frac{\cot\beta_2}{\cos\psi_2}$ in (19) simplify to the following for each edge:

$$\text{Edge 1:} \quad \frac{\sin\psi_{21}}{\sin\beta_{21}} = \frac{\cos\theta'}{\sin^2\theta'\cos^2\phi' + \cos^2\theta'} \tag{23a}$$

$$\cot\beta_{21}\cos\psi_{21} = \frac{-\sin^2\theta'\cos\phi'\sin\phi'}{\sin^2\theta'\cos^2\phi' + \cos^2\theta'} \tag{23b}$$

Edge 2:
$$\frac{\sin\psi_{22}}{\sin\beta_{22}} = \frac{\cos\theta'}{\sin^2\theta'\cos^2\phi' + \cos^2\theta'} \tag{23c}$$

$$\cot\beta_{22}\cos\psi_{22} = \frac{-\sin^2\theta'\cos\phi'\sin\phi'}{\sin^2\theta'\cos^2\phi' + \cos^2\theta'} \tag{23d}$$

Edge 3:
$$\frac{\sin\psi_{23}}{\sin\beta_{23}} = \frac{\cos\theta'}{\sin^2\theta'\sin^2\phi' + \cos^2\theta'} \tag{23e}$$

$$\cot\beta_{23}\cos\psi_{23} = \frac{\sin^2\theta'\cos\phi'\sin\phi'}{\sin^2\theta'\sin^2\phi' + \cos^2\theta'} \tag{23f}$$

Edge 4:
$$\frac{\sin\psi_{24}}{\sin\beta_{24}} = \frac{\cos\theta'}{\sin^2\theta'\sin^2\phi' + \cos^2\theta'} \tag{23g}$$

$$\cot\beta_{24}\cos\psi_{24} = \frac{\sin^2\theta'\cos\phi'\sin\phi'}{\sin^2\theta'\sin^2\phi' + \cos^2\theta'} \tag{23h}$$

The remaining factor in the equivalent currents equations that must be determined for each edge is $\underline{K}^f_2$. The preceding vectors and functions refer to the edge of second-order diffraction only. The vectors and functions involved in the definition of $\underline{K}^f_2$ involve the edge of first-order diffraction only except for the $|\hat{\sigma} \times \hat{t}_2|$ factor which involves directional vectors from the edges of both first- and second-order diffraction. For a half plane, $\underline{K}^f_2$ is given in (18).

The $\hat{t}_1$ and $\hat{n}_1$ vectors are defined for each edge in (3). The incident fields, $\underline{H}^i$ and $\underline{E}^i$ are defined in (9). F(x) is the modified Fresnel transtion function of (20c). The directional angles β_o' and ψ are the same as those introduced at the beginning of this section.

All the necessary functions of these angles derive easily from the relations of (4) and (5).

The unit vector in the direction of integration, $\hat{\sigma}$, for each edge is:

$$\text{Edge 1:} \quad \hat{\sigma}_1 = -\hat{a}_x \sin\beta_{o_1}' + \hat{a}_y \cos\beta_{o_1}' \tag{24a}$$

$$\text{Edge 2:} \quad \hat{\sigma}_2 = \hat{a}_x \sin\beta_{o_2}' - \hat{a}_y \cos\beta_{o_2}' \tag{24b}$$

$$\text{Edge 3:} \quad \hat{\sigma}_3 = -\hat{a}_x \cos\beta_{o_3}' - \hat{a}_y \sin\beta_{o_3}' \tag{24c}$$

$$\text{Edge 4:} \quad \hat{\sigma}_4 = \hat{a}_x \cos\beta_{o_4}' + \hat{a}_y \sin\beta_{o_4}' \tag{24d}$$

In general the term μ is defined as:

$$\mu = \frac{\cos\gamma - \cos^2\beta_o'}{\sin^2\beta_o'} \tag{25}$$

where

$$\cos\gamma = \hat{\sigma} \cdot \hat{s} \tag{26}$$

For each edge, the γ functions are:

$$\text{Edge 1:} \quad \cos\gamma_1 = -\sin\beta_{o_1}'\sin\theta'\cos\phi' + \cos\beta_{o_1}'\sin\theta'\sin\phi' \tag{27a}$$

$$\text{Edge 2:} \quad \cos\gamma_2 = \sin\beta_{o_2}'\sin\theta'\cos\phi' - \cos\beta_{o_2}'\sin\theta'\sin\phi' \tag{27b}$$

$$\text{Edge 3:} \quad \cos\gamma_3 = -\sin\beta_{o_3}'\sin\theta'\cos\phi' - \cos\beta_{o_3}'\sin\theta'\sin\phi' \tag{27c}$$

$$\text{Edge 4:} \quad \cos\gamma_4 = \sin\beta_{o_4}'\sin\theta'\cos\phi' + \cos\beta_{o_4}'\sin\theta'\sin\phi' \tag{27d}$$

Using these definitions and those of (4), the μ's for each edge are:

$$\text{Edge 1:} \quad \mu_1 = \frac{\cos\gamma_1 - \cos^2\beta_{o_1}'}{\sin^2\beta_{o_1}'} \tag{28a}$$

$$\text{Edge 2:} \quad \mu_2 = \frac{\cos\gamma_2 - \cos^2\beta_{o_2}'}{\sin^2\beta_{o_2}'} \tag{28b}$$

$$\text{Edge 3:} \quad \mu_3 = \frac{\cos\gamma_3 - \cos^2\beta_{o_3}'}{\sin^2\beta_{o_3}'} \tag{28c}$$

$$\text{Edge 4:} \quad \mu_4 = \frac{\cos\gamma_4 - \cos^2\beta_{o_4}'}{\sin^2\beta_{o_4}'} \tag{28d}$$

The coupling terms between the edge of first-order diffraction and the edge of second-order diffraction are the $|\hat{\sigma} \times \hat{t}_2|$, the L, and the $\mathcal{L}$ terms. For each pair of intersecting edges a different $\underline{K}_2^f$ factor results due to these terms. Due to symmetry, one needs to consider the range $0^\circ \leq \phi' \leq 90^\circ$ only for the plate rotation angle. This eliminates having to consider interactions between some edges. The remaining interactions that one must consider are:

(1) 1st-order diffraction from edge 1 to edge 4.

(2) 1st-order diffraction from edge 1 to edge 2.

(3) 1st-order diffraction from edge 2 to edge 4.

(4) 1st-order diffraction from edge 2 to edge 1.

(5) 1st-order diffraction from edge 3 to edge 2.

(6) 1st-order diffraction from edge 3 to edge 4.

(7) 1st-order diffraction from edge 4 to edge 2.

(8) 1st-order diffraction from edge 4 to edge 3.

The $|\hat{\sigma} \times \hat{t}_2|$ terms for each of these interactions reduce to:

$$\text{Edge 1 to Edge 4:} \quad |\hat{\sigma}_1 \times \hat{t}_{2_4}| = \cos\beta_{o_1}' \tag{29a}$$

$$\text{Edge 1 to Edge 2:} \quad |\hat{\sigma}_1 \times \hat{t}_{2_2}| = \sin\beta_{o_1}' \tag{29b}$$

$$\text{Edge 2 to Edge 4:} \quad |\hat{\sigma}_2 \times \hat{t}_{2_4}| = \cos\beta_{o_2}' \tag{29c}$$

Edge 2 to Edge 1: $|\hat{\sigma}_2 \times \hat{t}_{2_1}| = \sin\beta_{o_2}'$ (29d)

Edge 3 to Edge 2: $|\hat{\sigma}_3 \times \hat{t}_{2_2}| = \cos\beta_{o_3}'$ (29e)

Edge 3 to Edge 4: $|\hat{\sigma}_3 \times \hat{t}_{2_4}| = \sin\beta_{o_3}'$ (29f)

Edge 4 to Edge 2: $|\hat{\sigma}_4 \times \hat{t}_{2_2}| = \cos\beta_{o_4}'$ (29g)

Edge 4 to Edge 3: $|\hat{\sigma}_4 \times \hat{t}_{2_3}| = \sin\beta_{o_4}'$ (29h)

The distance parameter, ℓ, designates the distance from the point of first-order diffraction to the point of second-order diffraction measured along $\hat{\sigma}$, the grazing diffracted ray. The ℓ parameters are constant functions of incidence angle only for opposite edge interactions but are functions of distance along the edge for adjacent edge interactions. Fig. 5 shows the geometry for determining the ℓ parameters for interactions between edges 1 and 2 and edges 1 and 4. The geometries for the other interactions are similar. The limits of integration in the vector potential integrals of (15) vary according to the illumination of the edge of second-order diffraction. The extent of illumination is bounded by the grazing diffracted rays from the edge of first-order diffraction. Thus, the limits of integration are a function of the incidence angle. The distance parameters, ℓ and L, along with the limits of integration are given below for each pair of interacting edges. Recall that:

$$L = k\ell \sin^2\beta_o' \tag{30}$$

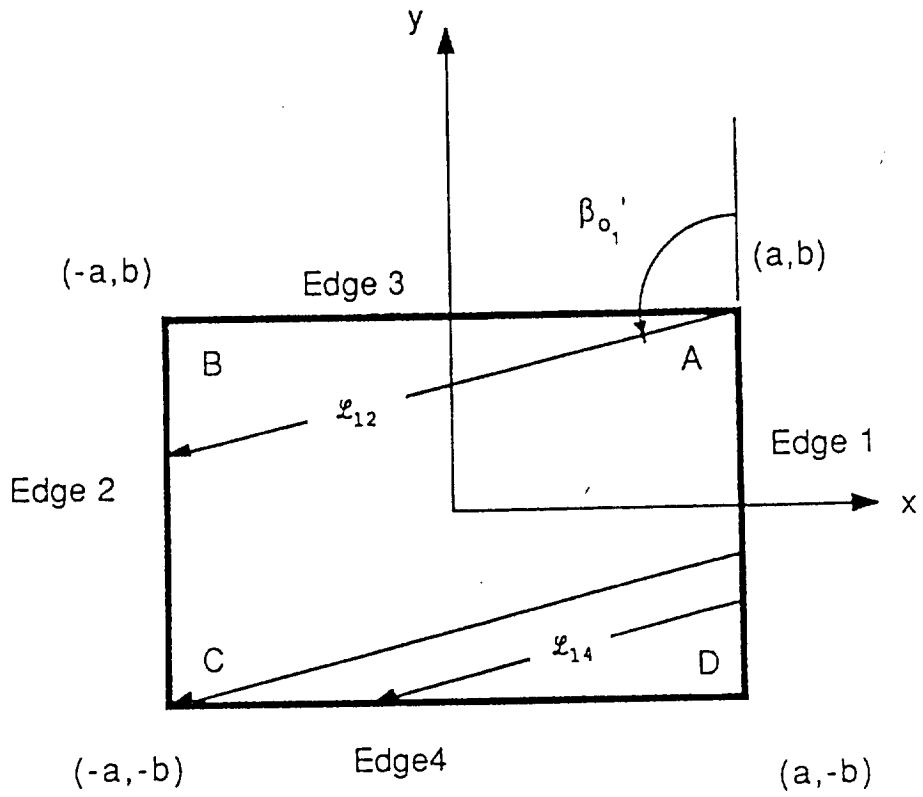

Fig. 5. Geometry for determining the distance parameters.

Edge 1 to Edge 4

$$\mathcal{L}_{14} = \frac{a - x_4}{\cos\beta_{o_1}'} \tag{31a}$$

$$L_{14} = k\mathcal{L}_{14}\sin^2\beta_{o_1}' \tag{31b}$$

Limits of integration: $-a \le x \le a$ for $\beta_{o_1}' \le \pi - \tan^{-1}(a/b)$

$a - 2b\tan(\pi-\beta_{o_1}') \le x \le a$ for $\beta_{o_1}' \ge \pi - \tan^{-1}(a/b)$

Edge 1 to Edge 2

$$\mathcal{L}_{12} = \frac{2a}{\cos\beta_{o_1}'} \tag{31c}$$

$$L_{12} = k\mathcal{L}_{12}\sin^2\beta_{o_1}' \tag{31d}$$

Limits of integration:

$$-b \le y \le b - \frac{2a}{\tan(\pi-\beta_{o_1}')} \quad \text{for } \beta_{o_1}' \le \pi - \tan^{-1}(a/b)$$

Edge 2 to Edge 4

$$\mathcal{L}_{24} = \frac{a + x_4}{\sin\beta_{o_2}'} \tag{31e}$$

$$L_{24} = k\mathcal{L}_{14}\sin^2\beta_{o_2}' \tag{31f}$$

Limits of integration: $-a \le x \le a$ for $\beta_{o_2}' \ge \tan^{-1}(a/b)$

$-a \le x \le -a + 2b\tan\beta_{o_2}'$ for $\beta_{o_2}' \ge \pi - \tan^{-1}(a/b)$

Edge 2 to Edge 1

$$\mathcal{L}_{21} = \frac{2a}{\sin\beta_{o_2}'} \tag{31g}$$

$$L_{21} = k\mathcal{L}_{21}\sin^2\beta_{o_2}' \tag{31h}$$

Limits of integration:

$$-b \le y \le b - \frac{2a}{\tan(\beta_{o_2}')} \quad \text{for } \beta_{o_2}' \le \tan^{-1}(a/b)$$

Edge 3 to Edge 2

$$\mathcal{L}_{32} = \frac{b - y_2}{\sin\beta_{o_2}'} \tag{31i}$$

$$L_{32} = k\mathcal{L}_{32}\sin^2\beta_{o_3}' \tag{31j}$$

Limits of integration: $-b \le y \le b$ for $\beta_{o_3}' \ge \tan^{-1}(b/a)$

$b - 2a\tan\beta_{o_3}' \le y \le b$ for $\beta_{o_3}' \ge \tan^{-1}(b/a)$

Edge 3 to Edge 4

$$\mathcal{L}_{34} = \frac{2b}{\sin\beta_{o_3}'} \tag{31k}$$

$$L_{34} = k\mathcal{L}_{34}\sin^2\beta_{o_3}' \tag{31l}$$

Limits of integration:

$$a - \frac{2b}{\tan\beta_{o_3}'} \le x \le a \qquad \text{for } \beta_{o_3}' \le \tan^{-1}(b/a)$$

Edge 4 to Edge 2

$$\mathcal{L}_{42} = \frac{b + y_2}{\cos\beta_{o_4}'} \tag{31m}$$

$$L_{42} = k\mathcal{L}_{42}\sin^2\beta_{o_4}' \tag{31n}$$

Limits of integration: $-b \le y \le b$ for $\beta_{o_4}' \le \pi - \tan^{-1}(b/a)$

$-b \le y \le -b + 2a\tan(\pi-\beta_{o_4}')$ for $\beta_{o_4}' \ge \tan^{-1}(b/a)$

Edge 4 to Edge 3

$$\mathcal{L}_{43} = \frac{2b}{\cos\beta_{o_4}'} \tag{31o}$$

$$L_{43} = k\mathcal{L}_{43}\sin^2\beta_{o_4}' \tag{31p}$$

Limits of integration:

$$a - \frac{2b}{\tan(\pi-\beta_{o_4}')} \le x \le a \qquad \text{for } \beta_{o_4}' \le \pi - \tan^{-1}(b/a)$$

The second-order fields are determined by substituting the current components for each pair of interacting edges into the vector potential equations of (11) and using (10). For opposite edges the integrals reduce to closed-form expressions. The adjacent-edge integrals must be evaluated numerically. Just as for the first-order diffractions, integration is with respect to either the x or y coordinate so that the integrals involved simplify to the following:

Edge 1 to Edge 4

$$I_{14}^{a} = \int_{x_1}^{x_2} e^{-jk\mathcal{L}_{14}} F(\sqrt{L_{14}(1-\mu_1)}) e^{jkx\sin\theta'\cos\phi'} dx \tag{32a}$$

$$I_{14}^{b} = \int_{x_1}^{x_2} e^{-jk\mathcal{L}_{14}} F(\sqrt{L_{14}(1+\cos\psi_1)}) e^{jkx\sin\theta'\cos\phi'} dx \tag{32b}$$

Edge 1 to Edge 2

$$I_{12} = -\int_{y_1}^{y_2} e^{j2ky\sin\theta'\sin\phi'} dy$$

$$= -2b\,\mathrm{sinc}(2kb\sin\theta'\sin\phi') - \frac{\exp\left(-j\frac{4ak}{\tan(\pi-\beta_{o_1'})}\sin\theta'\sin\phi'\right)}{j2k\sin\theta'\sin\phi'} \tag{32c}$$

Edge 2 to Edge 4

$$I_{24}^{a} = \int_{x_1}^{x_2} e^{-jk\mathcal{L}_{24}} F(\sqrt{L_{24}(1-\mu_2)}) e^{jkx\sin\theta'\cos\phi'} dx \tag{32d}$$

$$I_{24}^{b} = \int_{x_1}^{x_2} e^{-jk\mathcal{L}_{24}} F(\sqrt{L_{24}(1+\cos\psi_2)}) e^{jkx\sin\theta'\cos\phi'} dx \tag{32e}$$

Edge 2 to Edge 1

$$I_{21} = \int_{y_1}^{y_2} e^{j2ky\sin\theta'\sin\phi'}\, dy$$

$$= 2b\,\mathrm{sinc}(2kb\sin\theta'\sin\phi') + \frac{\exp\left(-j\,\frac{4ak}{\tan\beta_{o_2'}}\sin\theta'\sin\phi'\right)}{j2k\,\sin\theta'\,\sin\phi'} \qquad (32f)$$

Edge 3 to Edge 2

$$I_{32}^{a} = -\int_{y_1}^{y_2} e^{-jk\mathcal{L}_{32}}\, F\left(\sqrt{L_{32}(1-\mu_3)}\right)\, e^{jky\sin\theta'\sin\phi'}\, dy \qquad (32g)$$

$$I_{32}^{b} = -\int_{y_1}^{y_2} e^{-jk\mathcal{L}_{32}}\, F\left(\sqrt{L_{32}(1+\cos\psi_3)}\right)\, e^{jky\sin\theta'\sin\phi'}\, dy \qquad (32h)$$

Edge 3 to Edge 4

$$I_{34} = \int_{x_1}^{x_2} e^{j2kx\sin\theta'\cos\phi'}\, dx$$

$$= -\frac{\exp\left(-j\,\frac{4bk}{\tan\beta_{o_3'}}\sin\theta'\cos\phi'\right)}{j2k\,\sin\theta'\,\cos\phi'} \qquad (32i)$$

Edge 4 to Edge 2

$$I_{42}^{a} = -\int_{y_1}^{y_2} e^{-jk\mathcal{L}_{42}}\, F\left(\sqrt{L_{42}(1-\mu_4)}\right)\, e^{jky\sin\theta'\sin\phi'}\, dy \qquad (32j)$$

$$I_{42}^{b} = -\int_{y_1}^{y_2} e^{-jk\mathcal{L}_{42}}\, F\left(\sqrt{L_{42}(1+\cos\psi_4)}\right)\, e^{jky\sin\theta'\sin\phi'}\, dy \qquad (32k)$$

Edge 4 to Edge 3

$$I_{34} = \int_{x_1}^{x_2} e^{j2kx\sin\theta'\sin\phi'}\, dx$$

$$= -\frac{\exp\left(\,j\,\frac{4kb}{\tan(\pi-\beta_{o_4'})}\sin\theta'\cos\phi'\,\right)}{j2k\,\sin\theta'\,\cos\phi'} \qquad (32l)$$

B. Corner Diffraction

Because the GTD and UTD diffraction coefficients are derived from the exact solution to scattering by an infinite wedge, the coefficients fail to account for the joining of two edges at a corner. For certain aspect angles, the scattering from the corners is significant. Pathak and Burnside developed a heuristic corner diffraction coefficient [7]-[8] based upon an appropriate, although non-rigorous, modification of an asymptotic evaluation of the radiation integral due to the equivalent edge current that would exist along the scattering edge if the corner were not present. One major flaw in the coefficient is that it is non-unique for certain backscatter angles near normal incidence [9], thus a rigorously-developed corner diffraction coefficient is desirable. However, Pathak and Burnside's coefficient is successful for many plate geometries and may be used with caution.

The geometry for a corner in a planar surface is shown in Fig. 6. The total diffracted field from one corner is the sum of contributions from each of the edges comprising the corner. The general form of the corner diffracted field is:

$$\underline{E}^c(s) = -\underline{E}^i(Q_c)\cdot\tilde{D}_c\sqrt{\frac{s'}{s''(s'+s'')}}\sqrt{\frac{s(s+s_c)}{s_c}}\;\frac{e^{-jks}}{s} \tag{33}$$

where

$\underline{E}^i(Q_c)$ = the incident field at the corner.

$\tilde{D}_c$ = the dyadic corner diffraction coefficient.

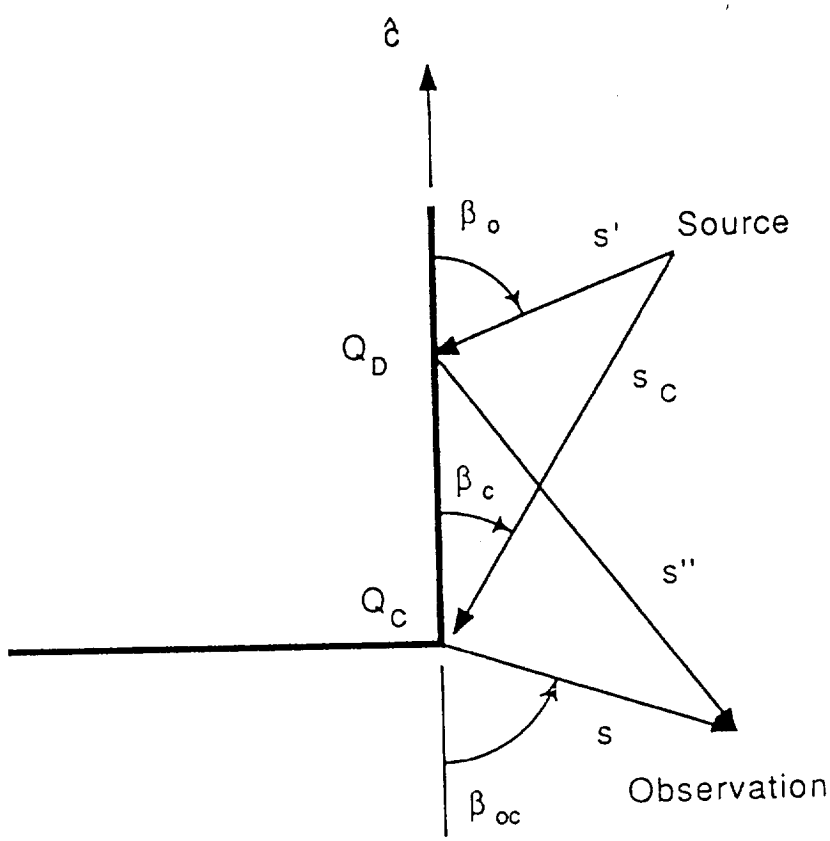

Fig. 6. Geometry for a corner in a planar surface.

s = the distance from the corner to the receiver.

s′ = the distance from the source to the point of edge diffraction.

s" = the distance from the point of edge diffraction to the receiver.

s_c = the distance from the source to the corner.

e^{-jks} = the phase factor.

The dyadic corner diffraction coefficient, like the ordinary diffraction coefficient, is in terms of parallel and perpendicular components:

$$\tilde{D}_c = \hat{e}_h^i \, \hat{e}_h^{dc} \, D_h^c + \hat{e}_s^i \, \hat{e}_s^{dc} \, D_s^c \tag{34}$$

D_h^c and D_s^c are the hard and soft corner diffraction coefficients, respectively, given by the following:

$$D_{s,h}^c = \frac{e^{-j\pi/4}}{\sqrt{2\pi k}} C_{s,h}(Q_E) \frac{\sqrt{\sin\beta_o \sin\beta_{oc}}}{\cos\beta_{oc} - \cos\beta_c} F[kL_c a(\pi+\beta_{oc} - \beta_c)] \tag{35}$$

where

$$C_{s,h}(Q_E) = \frac{-e^{-j\pi/4}}{2\sqrt{2\pi k}\,\sin\beta_o} \times$$

$$\left\{ \frac{F[kLa(\beta^-)]}{\cos(\beta^-/2)} \left| F\left[\frac{La(\beta^-)/\lambda}{kL_c a(\pi+\beta_{oc} - \beta_c)} \right] \right| \right.$$

$$\left. \mp \frac{F[kLa(\beta^+)]}{\cos(\beta^+/2)} \left| F\left[\frac{La(\beta^+)/\lambda}{kL_c a(\pi+\beta_{oc} - \beta_c)} \right] \right| \right\} \tag{36}$$

F is the Fresnel transition function given by:

$$F(x) = 2j\sqrt{x}\, e^{jx} \int_{\sqrt{x}}^{\infty} e^{-j\tau^2}\, d\tau \tag{37}$$

$\beta^{\pm}$ are as:

$$\beta^{\pm} = \psi \pm \psi' \tag{38}$$

β_o is the Keller cone angle. The other angles and functions are:

β_c = the angle between the incident ray at the corner and the edge of interest.

β_{oc} = the angle between the diffracted ray at the corner and the extension of the edge of interest as shown in Fig. 3-5.

$$a(\psi) = 2\cos^2(\psi/2) \tag{39a}$$

$$L = \frac{s's''}{(s'+s'')} \sin^2(\beta_o) \tag{39b}$$

$$L_c = \frac{s_c s}{s_c+s} \tag{39c}$$

These fields simplify considerably for far-field, plane-wave scattering from the rectangular plate.

The RCS of the flat plate in all planes can be determined using only the corner diffraction coefficient. Near and at normal incidence, this formulation fails due to the nonreciprocal nature of the corner diffraction coefficient. To alleviate this problem, near and at normal incidence, the GTD equivalent currents solution is used; and the corner diffraction results are used away from the problem area. The total scattered field from a corner consists of terms for

each of the adjoining edges; therefore, eight terms are needed for the rectangular plate.

The general expression for the corner diffracted field due to one of the two adjoining edges is given in (33). For far-field scattering, $s \cong s_c \cong s' \cong s'' \cong \infty$; therefore:

$$\underline{E}^c(s) = -\underline{E}^i(Q_c) \cdot \tilde{D}_c \frac{e^{-jks}}{s} \tag{41}$$

for far-field scattering.

For far-field backscattering, $L_c = \infty$ so that:

$$F[kL_c a(\pi+\beta_{oc}-\beta_c)] \cong 1 \tag{42}$$

Also, $\beta_{oc} = \pi - \beta_c$ and $\psi' = \psi$ so that:

$$\frac{\sqrt{\sin\beta_c \sin\beta_{oc}}}{\cos\beta_{oc} - \cos\beta_c} = \frac{-\tan\beta_o}{2} \tag{43}$$

The diffraction coefficient simplifies to:

$$D^c_{s,h} = \frac{-e^{-j\pi/4}}{\sqrt{2\pi k}} C_{s,h}(Q_E) \frac{\tan\beta_o}{2} \tag{44}$$

For far-field backscattering, $L \cong L_c \cong \infty$ and $C_{s,h}(Q_E)$ simplifies to:

$$C_{s,h}(Q_E) = \frac{-e^{-j\pi/4}}{2\sqrt{2\pi k}\sin\beta_o} \left\{ \left| F\left(\frac{1}{2\pi\cos^2(\pi-\beta_o)} \right) \right| \mp \frac{1}{\cos\psi} \left| F\left(\frac{1}{2\pi\cos^2(\pi-\beta_o)} \right) \right| \right\} \tag{45}$$

The total field scattered due to one edge adjoining at a corner simplifies to:

$$\underline{E}^{c}_{s,h}(s) = E^{i}(Q_c)\,\frac{j}{8\pi k\cos\beta_o}\left(\frac{e^{-jks}}{s}\right)\times$$

$$\left\{\left|F\left(\frac{1}{2\pi\cos^2\beta_o}\right)\mp\frac{1}{\cos\psi}\left|F\left(\frac{\cos^2\psi}{2\pi\cos^2\beta_o}\right)\right|\right\} \qquad (46)$$

The top view of the plate geometry for the corner diffraction analysis is shown in Fig. 7. The incident fields are the same as in (9). The field must be determined at the corner of interest. The corners are designated as the following:

Corner A:	x = a	y = b
Corner B:	x = -a	y = b
Corner C:	x = -a	y = -b
Corner D:	x = a	y = -b

The angles ψ are the same as those given in (5). The ψ angle used for the scattering component for a designated edge and corner is the ψ associated with the edge. For example, the ψ_1 angle is used for scattering from corner A due to the presence of edge 1.

The β_o angle is the angle between the $-\hat{s}'$ and the edge or:

$$\cos\beta_o = -\hat{s}' \cdot \hat{c} \qquad (47)$$

where

$\hat{c}$ = the unit vector tangent to the edge of interest pointing outward from the corner of interest.

The vectors and angular functions for each corner/edge combination are:

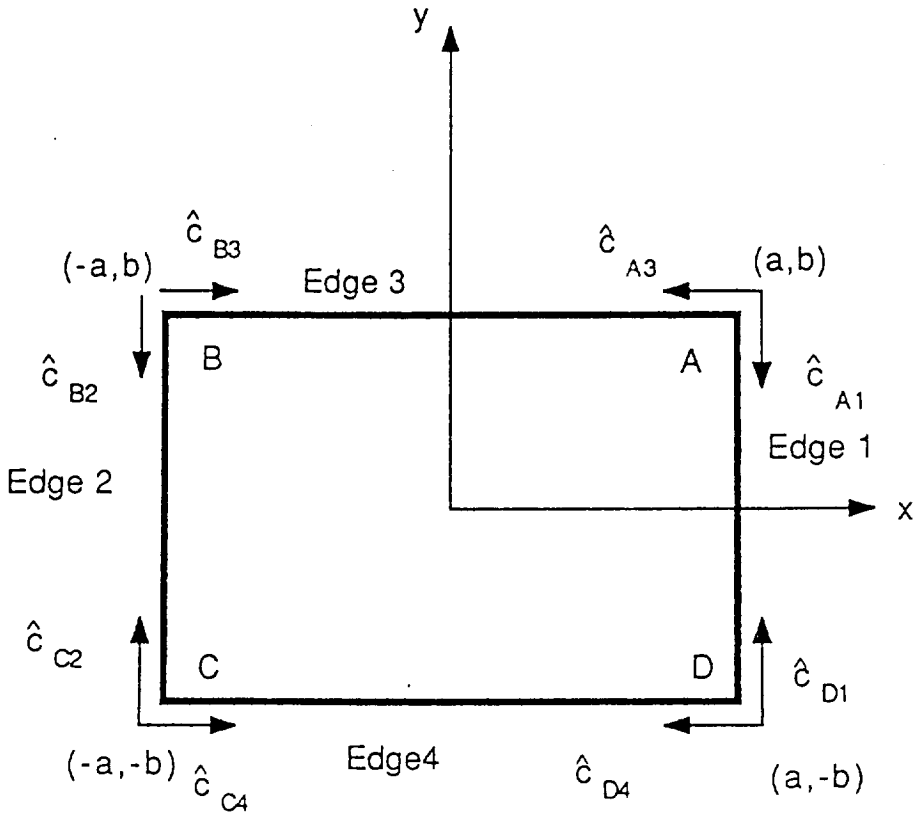

Fig. 7. Top view of the plate for the corner diffraction analysis.

Corner A

Edge 1: $\hat{c}_{A1} = -\hat{a}_y \qquad \cos\beta_{o_{A1}} = -\sin\theta'\sin\phi'$ (48a)

Edge 3: $\hat{c}_{A3} = -\hat{a}_x \qquad \cos\beta_{o_{A3}} = -\sin\theta'\cos\phi'$ (48b)

Corner B

Edge 2: $\hat{c}_{B2} = -\hat{a}_y \qquad \cos\beta_{o_{B2}} = -\sin\theta'\sin\phi'$ (48c)

Edge 3: $\hat{c}_{B3} = \hat{a}_x \qquad \cos\beta_{o_{B3}} = \sin\theta'\cos\phi'$ (48d)

Corner C

Edge 2: $\hat{c}_{C2} = \hat{a}_y \qquad \cos\beta_{o_{C2}} = \sin\theta'\sin\phi'$ (48e)

Edge 4: $\hat{c}_{C4} = \hat{a}_x \qquad \cos\beta_{o_{C4}} = \sin\theta'\cos\phi'$ (48f)

Corner D

Edge 1: $\hat{c}_{D1} = \hat{a}_y \qquad \cos\beta_{o_{D1}} = \sin\theta'\sin\phi'$ (48g)

Edge 4: $\hat{c}_{D4} = \hat{a}_x \qquad \cos\beta_{o_{D4}} = -\sin\theta'\cos\phi'$ (48h)

The final parameter that must be designated is s, the distance from the corner to the observation point. The geometry indicating these distances is in Fig. 8. For far-field scattering, the following approximations are used:

Amplitude: $s_A \cong s_B \cong s_C \cong s_D \cong s$ (49a)

Phase: $s_A \cong s - \frac{\sin\theta'}{2}\sqrt{2(a^2+b^2)}\,(\cos\phi'+\sin\phi')$ (49b)

$s_B \cong s - \frac{\sin\theta'}{2}\sqrt{2(a^2+b^2)}\,(\sin\phi'-\cos\phi')$ (49c)

$s_C \cong s + \frac{\sin\theta'}{2}\sqrt{2(a^2+b^2)}\,(\cos\phi'+\sin\phi')$ (49d)

$s_D \cong s - \frac{\sin\theta'}{2}\sqrt{2(a^2+b^2)}\,(\cos\phi'-\sin\phi')$ (49f)

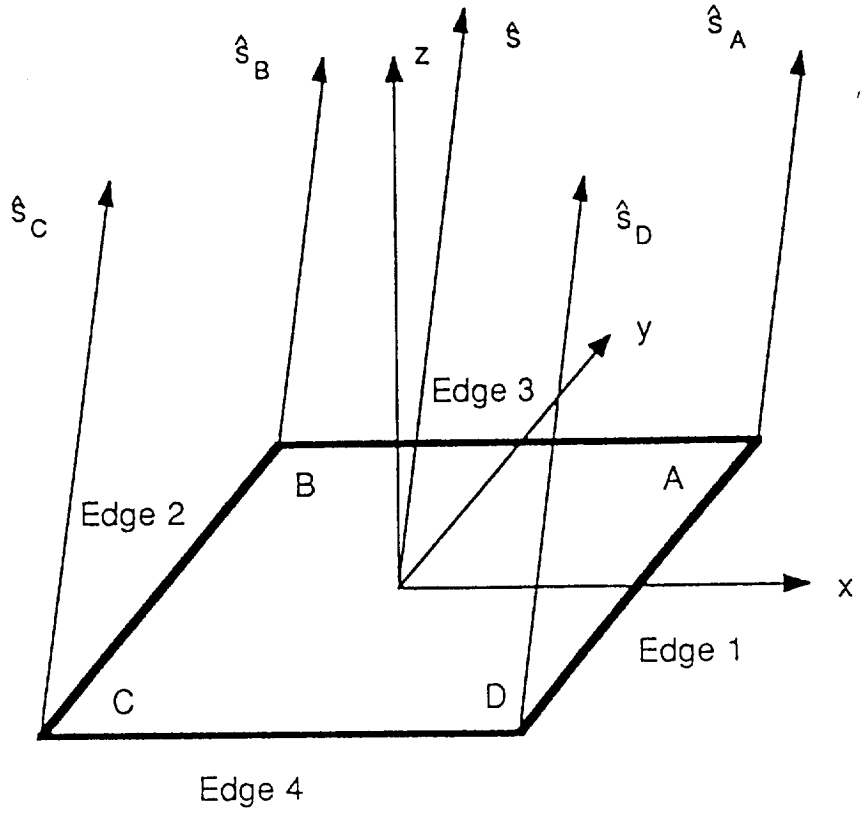

Fig. 8. Three-dimensional view of the plate for corner diffraction.

The total field scattered by the plate consists of a term of the form of (46) for each edge joined at a corner. These eight terms are added to arrive at the total field.

III. Results

Computations were made for a square plate with each side equal to 5.73 λ. Comparisons are made among the following: MM and experimental results, the PO equivalent currents model, the GTD equivalent currents model, the PO/PTD equivalent currents model, the PO/PTD/2nd-order equivalent currents model, and the corner diffraction coefficients model.

Fig. 9 shows soft polarization results for a 30° rotated plate. Even the PO equivalent currents, which account only for surface scattering, give good results near normal incidence. As the angle of incidence moves away from normal, there is a need for components to account for edge diffraction. The GTD and PO/PTD models greatly improve the results in the grazing regions, although there remains some disagreement which points to the necessity for higher-order and corner diffraction components. Fig. 10 shows results from the PO/PTD model with the second-order PTD coefficients added and also shows results from the corner diffraction coefficient model. Since the corner diffraction coefficients are inaccurate near and at normal incidence, the GTD equivalent currents solution is used in the region ±5° on either side of the normal direction and the corner diffraction solution is used elsewhere. The second-order currents do not improve the results for this case and even result in worse agreement than that

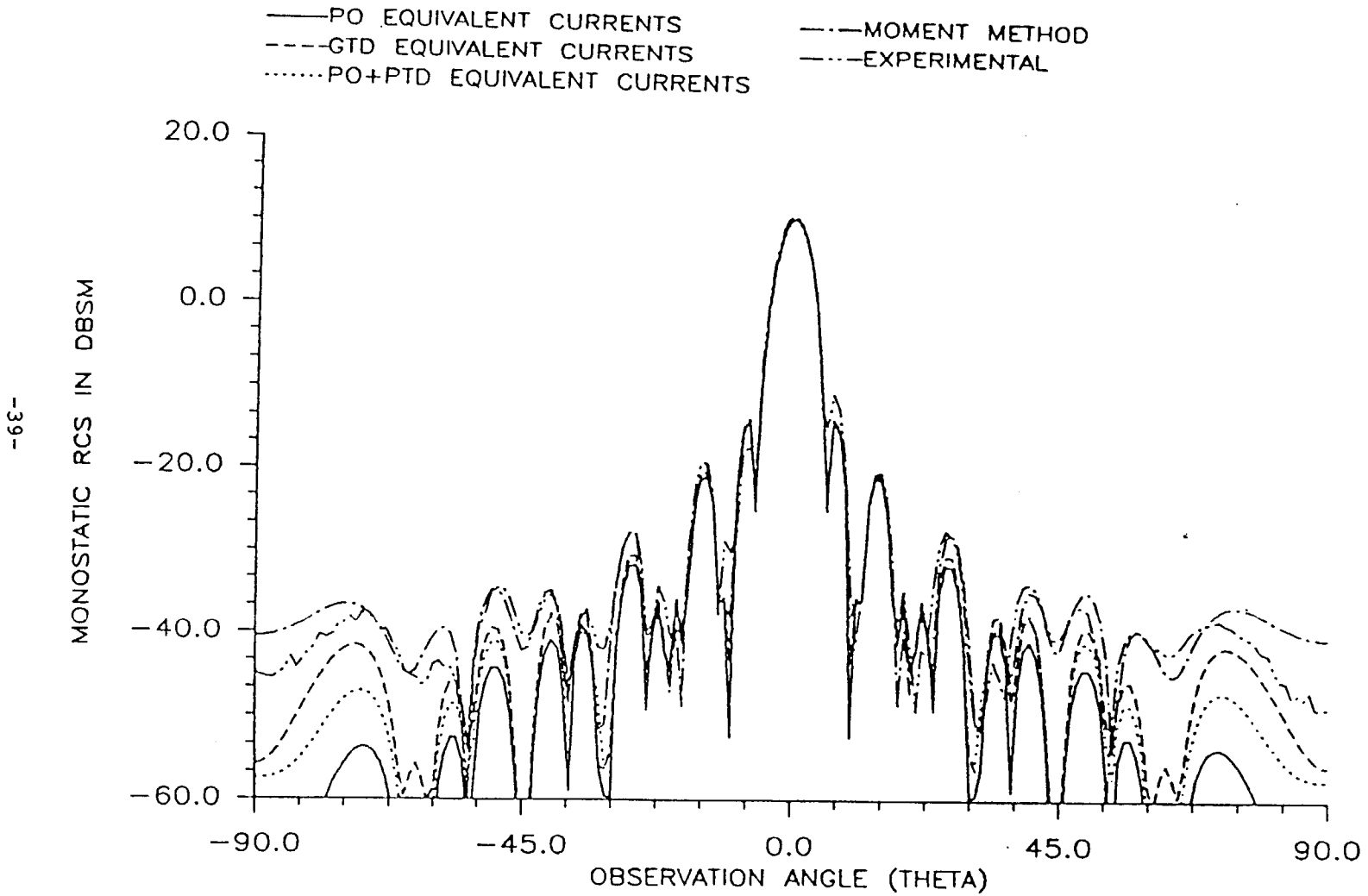

Fig. 9. Monostatic RCS of a square plate (soft polarization, 2a=2b=17.18 cm, f=10 GHz, $\phi'=30^{\circ}$).

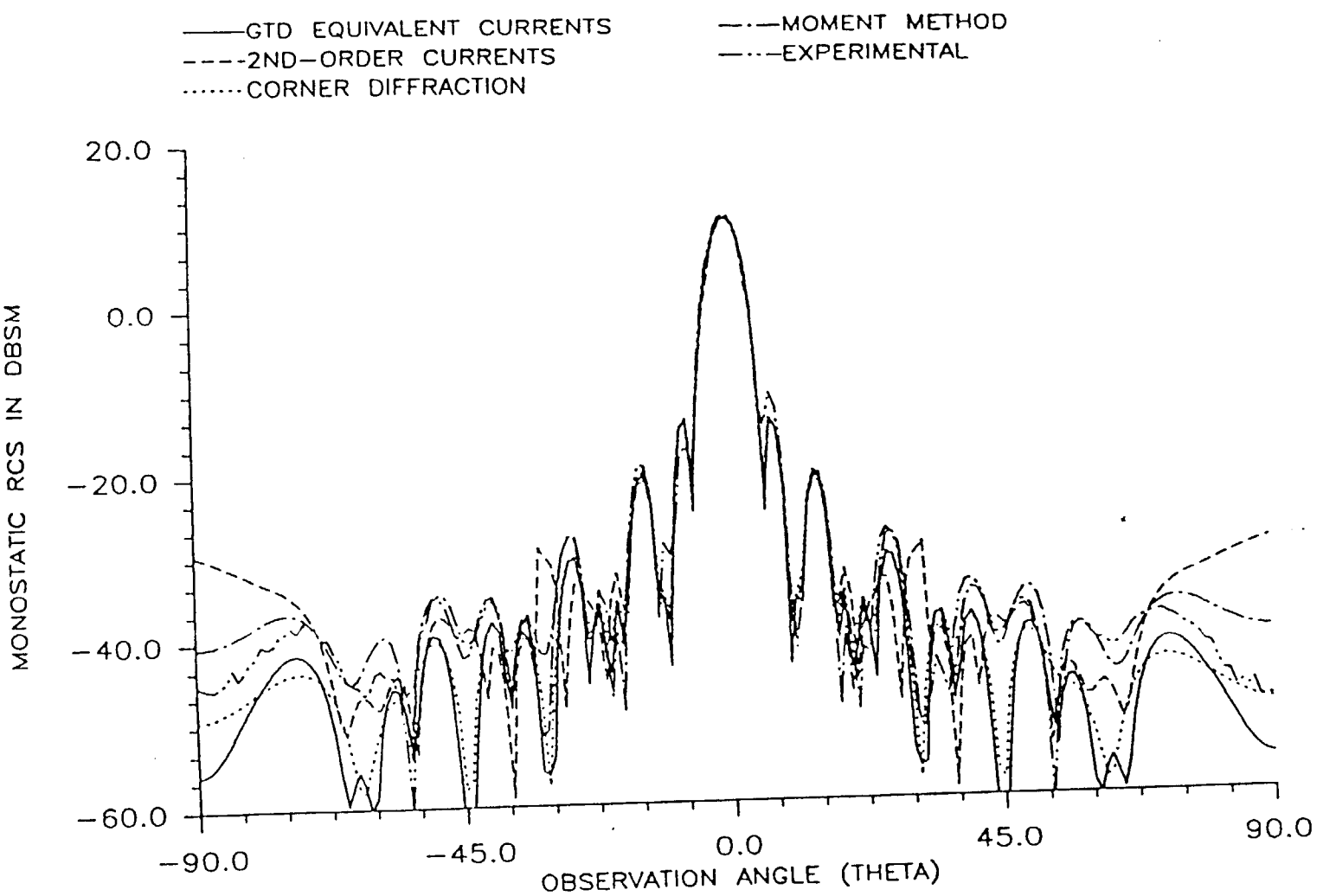

Fig. 10. Monostatic RCS of a square plate (soft polarization, 2a=2b=17.18 cm, f=10 GHz, $\phi'=30^{\circ}$).

obtained using the first-order models. The corner diffraction model improves the results near grazing and agrees with the first-order models away from grazing, indicating that the corner diffraction mechanism is the more crucial scattering mechanism for this plate rotation and polarization.

Fig. 11 shows the hard polarization results using the first-order models for the same plate configuration rotated 30°. Near and at grazing there is a major discrepancy between the first-order, high-frequency models and the experimental and MM results. The PO/PTD models with the second-order components added and the corner diffraction coefficients model yield much better results although discrepancies still exist. These results are displayed in Fig. 12.

The soft polarization results for the same size plate rotated 45° are in Fig. 13. One would expect that corner-diffraction would play a major role at this angle of rotation so that the large discrepancies of the first-order models near grazing incidence are not surprising. The addition of second-order equivalent currents yields excellent results in this case. Surprisingly, the corner diffraction model does not improve the results. These results, shown in Fig. 14, indicate that for this angle of rotation and polarization second-order components are the major contributing factors.

Hard plarization results for the same rotation angle are shown in Figs. 15 and 16. Just as for the 30° rotated plate for hard

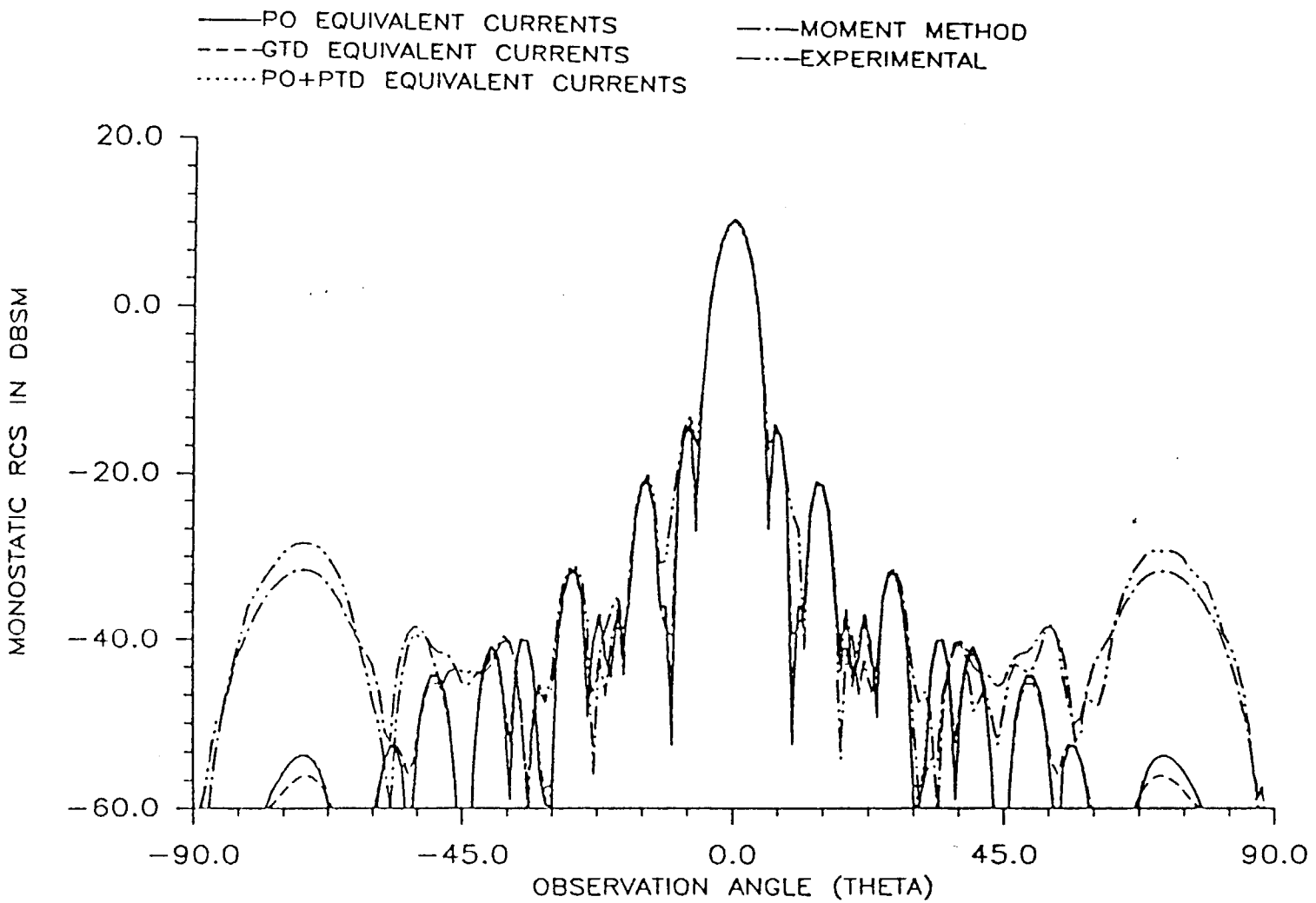

Fig. 11. Monostatic RCS of a square plate (hard polarization, 2a=2b=17.18 cm, f=10 GHz, $\phi'=30^{\circ}$).

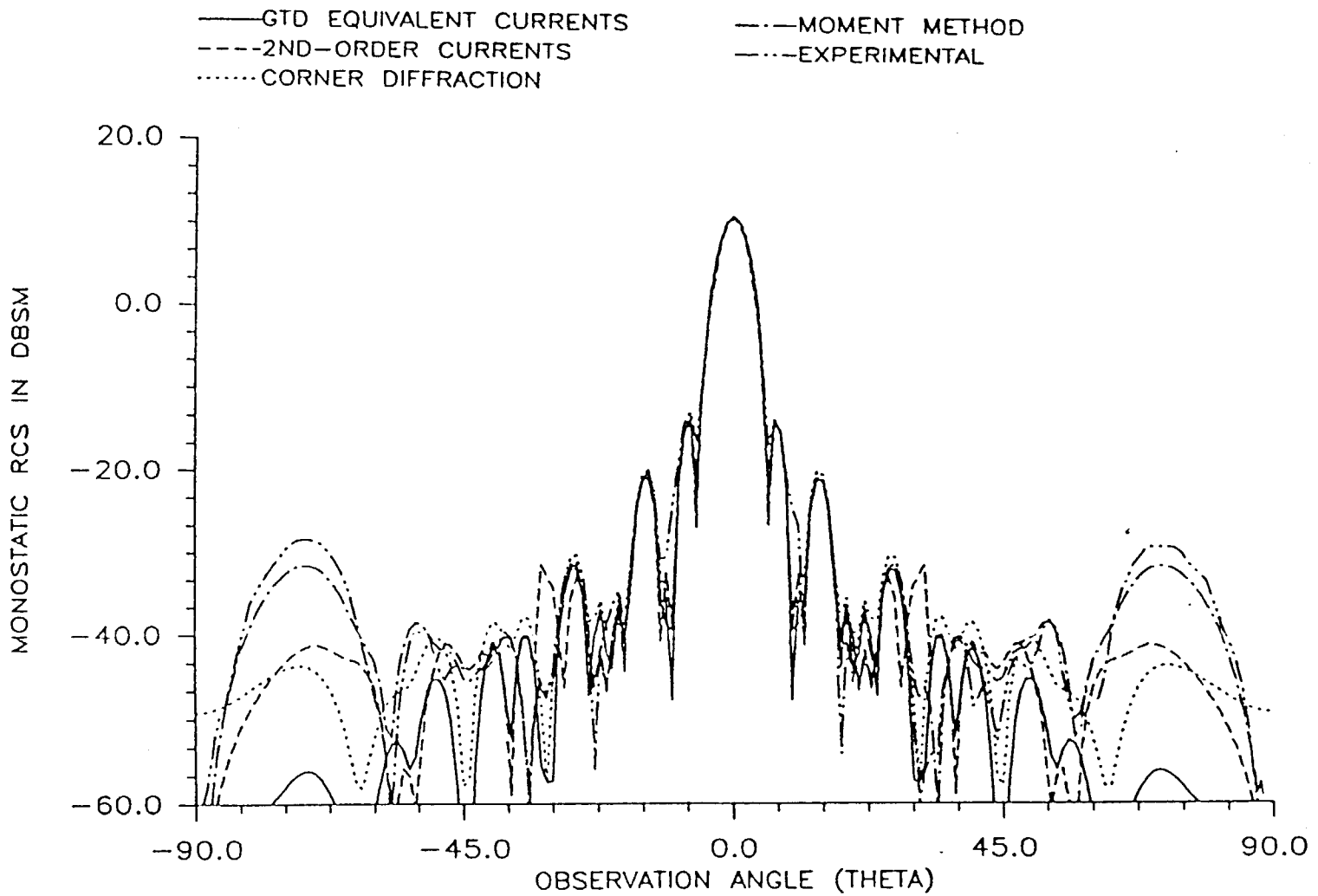

Fig. 12. Monostatic RCS of a square plate (hard polarization, 2a=2b=17.18 cm, f=10 GHz, $\phi'=30^{\circ}$).

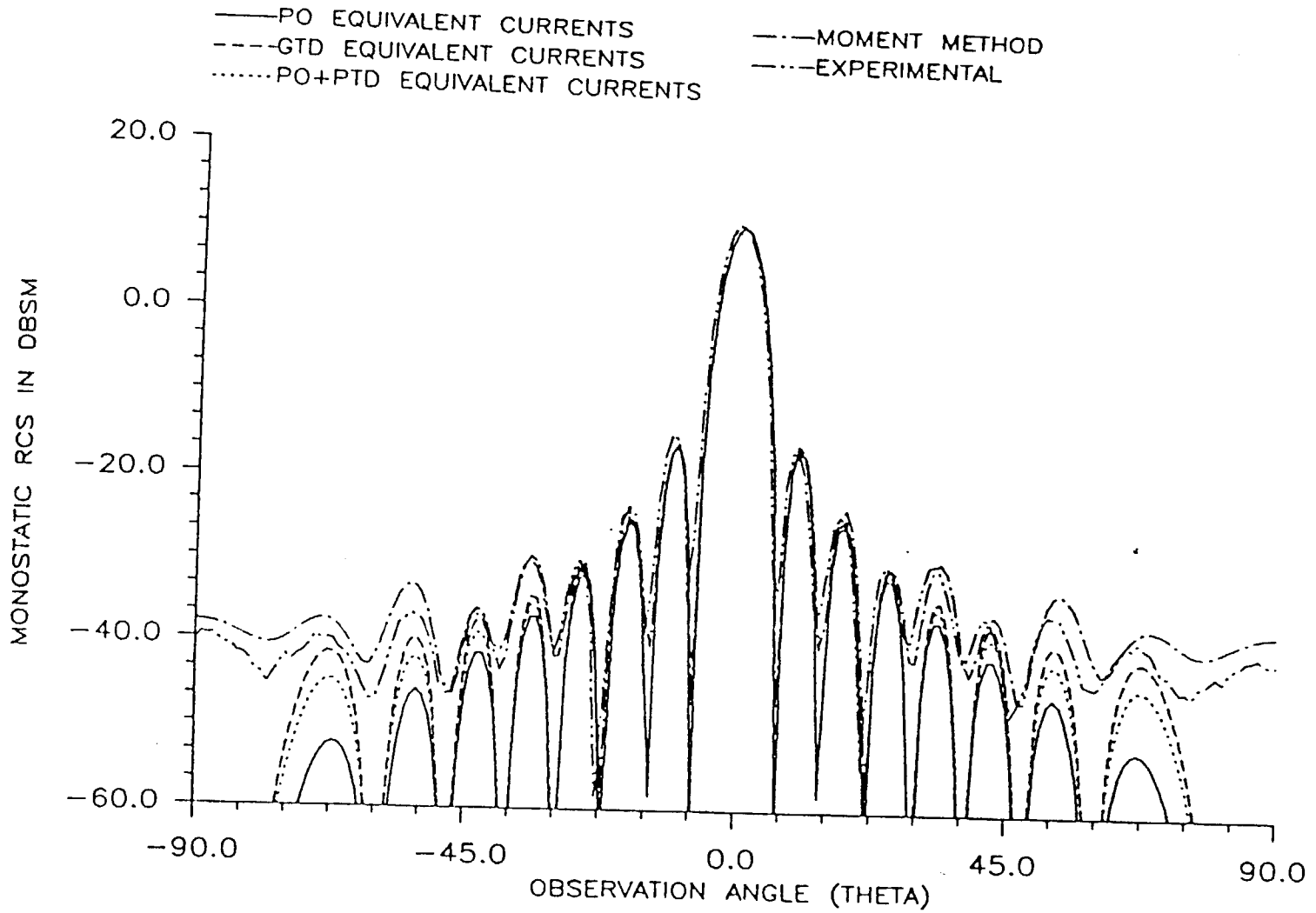

Fig. 13. Monostatic RCS of a square plate (soft polarization, 2a=2b=17.18 cm, f=10 GHz, $\phi'=45^{\circ}$).

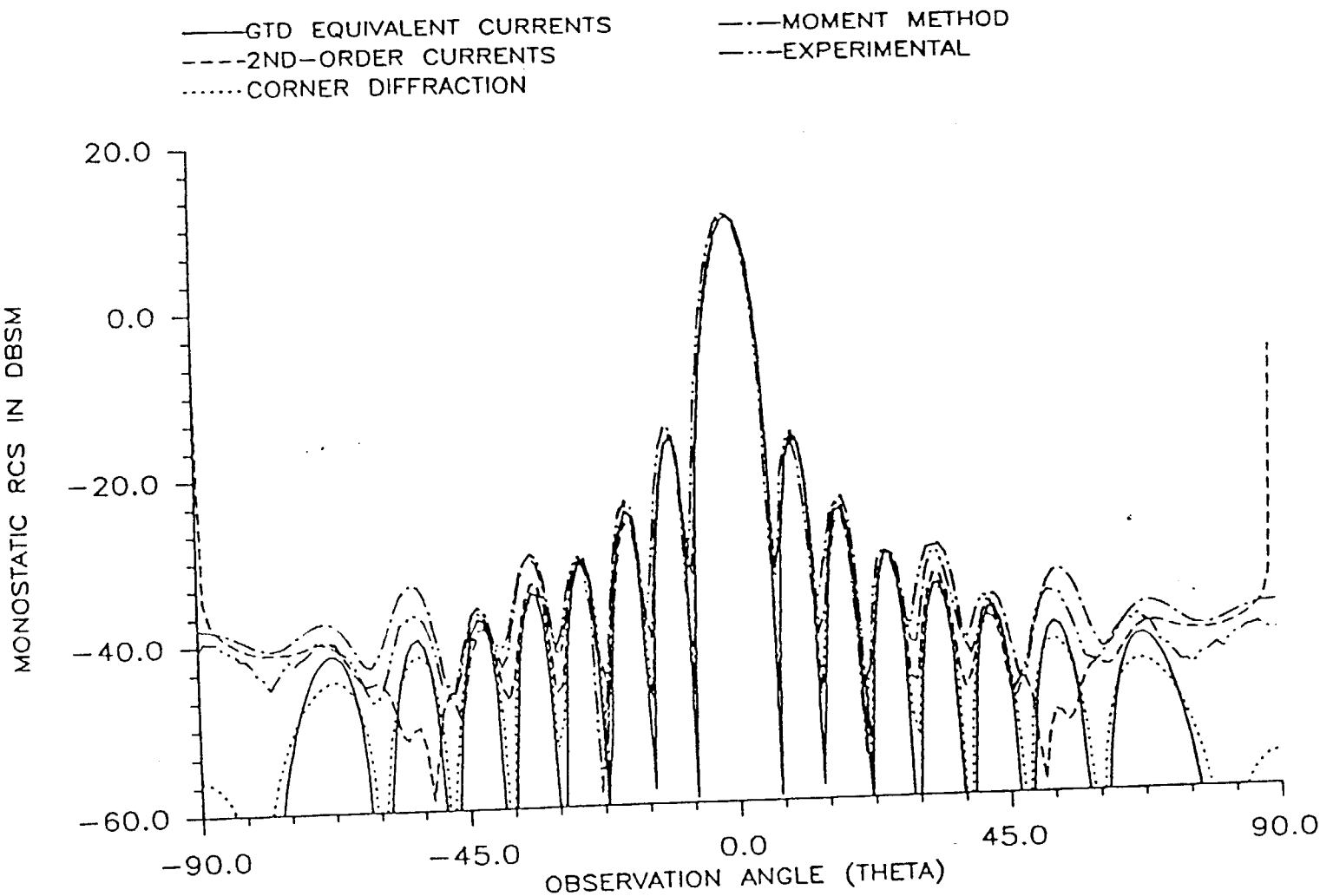

Fig. 14. Monostatic RCS of a square plate (soft polarization, 2a=2b=17.18 cm, f=10 GHz, $\phi'=45^{\circ}$).

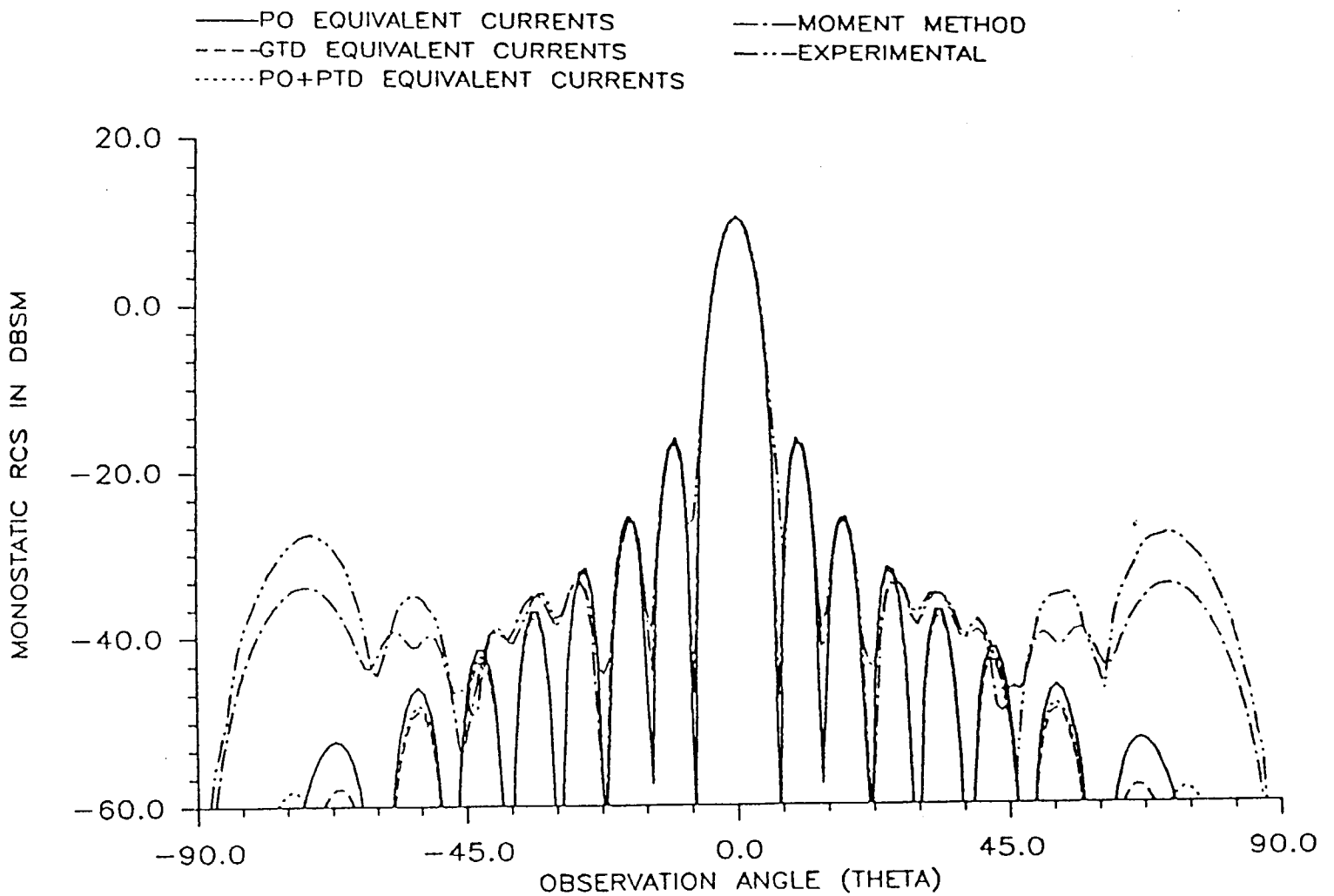

Fig. 15. Monostatic RCS of a square plate (hard polarization, 2a=2b=17.18 cm, f=10 GHz, $\phi'=45^{\circ}$).

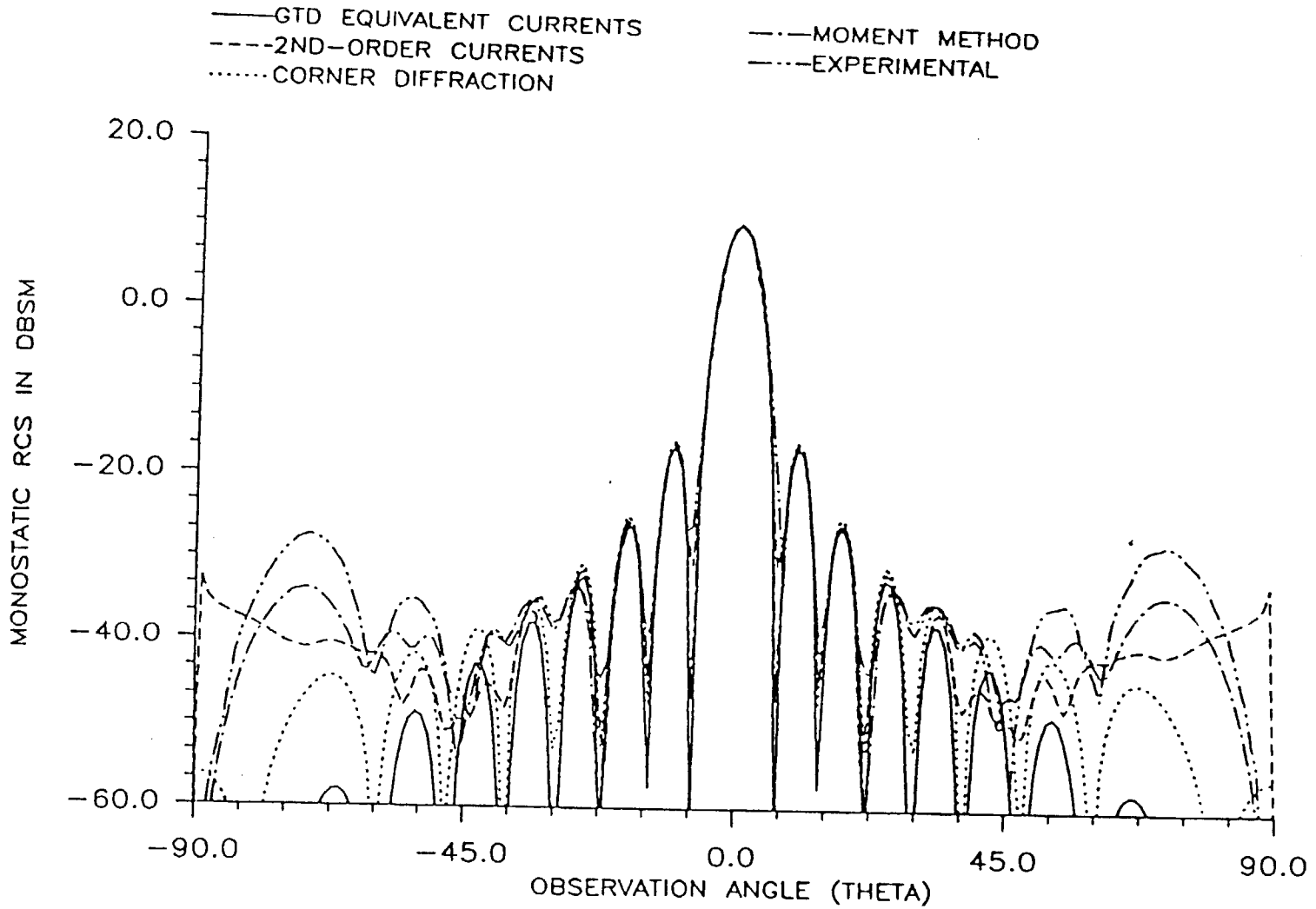

Fig. 16. Monostatic RCS of a square plate (hard polarization, 2a=2b=17.18 cm, f=10 GHz, $\phi'=45^{o}$).

polarization, the first-order, high-frequency models do not produce good results near the grazing regions. The corner diffraction model greatly improves the results; however, the addition of second-order components does not result in an improved model. This indicates that the corner diffraction mechanism is dominant for this configuration.

IV. Conclusions

The nonprincipal-plane scattering from a rectangular flat plate was considered. Comparisons among five high-frequency models, MM and experimental results were made. Near normal incidence all the models agreed; however, near grazing incidence a need for higher-order and corner diffraction mechanisms was noted. In many instances the second-order and corner-scattered fields formulated in this report improved the results.

REFERENCES

[1] C. A. Balanis and L. A. Polka, "Nonprincipal plane scattering of flat plates," Semiannual Report, Grant No. NAG-1-562, National Aeronautics and Space Administration, Langley Research Center, Hampton, VA, Jan. 31, 1989.

[2] A. Michaeli, "Equivalent edge currents for arbitrary aspects of observation," *IEEE Trans. Antennas Propagat.*, vol. AP-32, pp. 252-258, Mar. 1984.

[3] ———, "Correction to 'Equivalent edge currents for arbitrary aspects of observation'," *IEEE Trans. Antennas Propagat.*, vol. AP-33, no. 2, p. 227, Feb. 1985.

[4] ———, "Elimination of infinities in equivalent edge currents, part II: physical optics components," *IEEE Trans. Antennas Propagat.*, vol. AP-34, pp. 1034-1037, Aug. 1986.

[5] ———, "Elimination of infinities in equivalent edge currents, part I: Fringe current components," *IEEE Trans. Antennas Propagat.*, vol. AP-34, pp. 912-918, July 1986.

[6] ———, "Equivalent currents for second-order diffraction by the edges of perfectly conducting polygonal surfaces," *IEEE Trans. Antennas Propagat.*, vol. AP-35, pp. 183-190, Feb. 1987.

[7] F. A. Sikta, W. D. Burnside, T. Chu, and L. Peters, Jr., "First-order equivalent current and corner diffraction scattering from flat-plate structures," *IEEE Trans. Antennas Propagat.*, vol. AP-31, pp. 584-589, July 1983.

[8] P. H. Pathak, "Techniques for High Frequency Problems," in *Antenna Handbook: Theory, Applications, and Design*, Y. T. Lo, S. W. Lee, Eds. New York: Van Nostrand Reinhold, 1988.

[9] A. Michaeli, "Comments on 'First-order equivalent current and corner diffraction scattering from flat plate structures,'" *IEEE Trans. Antennas Propagat.*, vol. AP-32, pp. 1011-1012, Sept. 1984.

PART B

PATTERN CONTROL OF HORN ANTENNAS

PART B

PATTERN CONTROL OF HORN ANTENNAS

I. Tasks Accomplished

During this period, the computations of the impedance elements have been completed. These include interactions between the two electric current modes, the electric current mode and the magnetic current mode, and the two magnetic current modes. Especially, an accurate and efficient formulation of computing interactions between electric current mode and magnetic current mode has been accomplished. This, together with other subroutines we have developed, enables us to fill-in all the elememt in the matrix.

After the fill-in of the impedance elements in the matrix, the forward problem is accomplished. That is, given the specification of the horn and the excitating waveguide mode, the radiation pattern of the antenna based on the integral equation can be obtained.

An example case was run for a standard X-band gain-horn (DBG-520) with the configuration in Figure 1. The H- and E-plane patterns of this horn antenna with perfectly conducting walls are shown respectively in Figures 2 and 3. Comparison with the gain pattern available from the manufacturer for up to the first side lobe shows

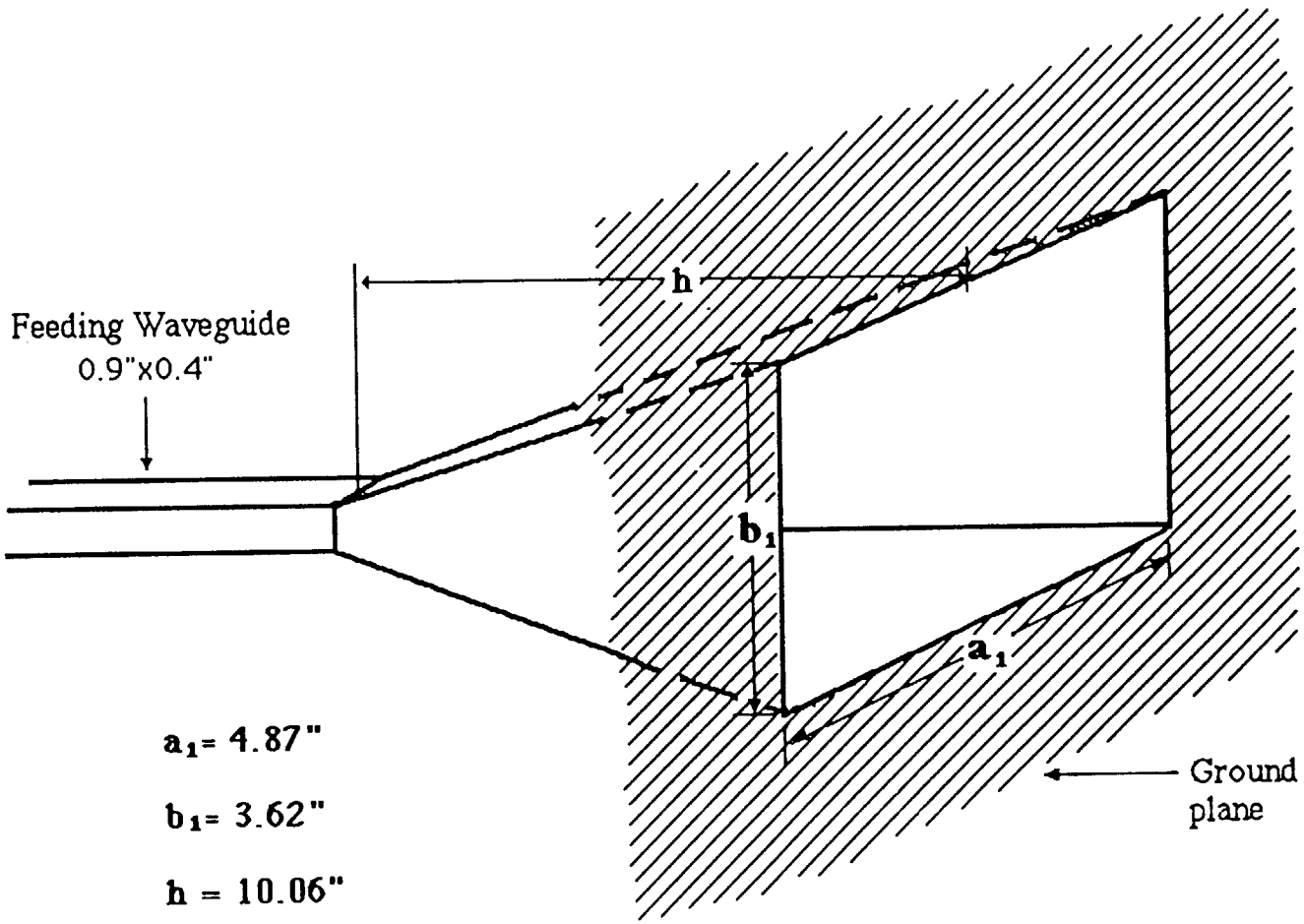

Figure 1. Geometry of the X-band horn (20dB gain, Model DBG-520)

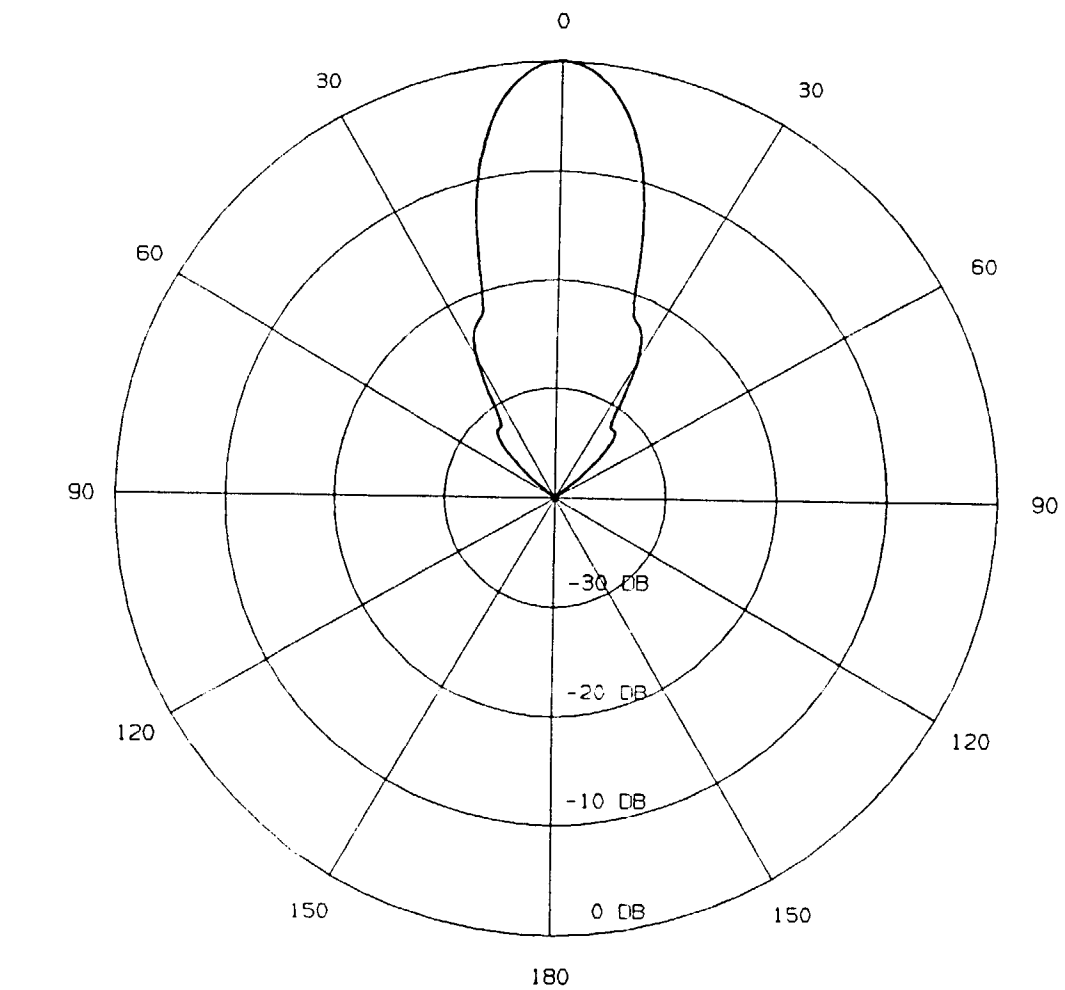

Figure 2. Normalized amplitude pattern for 20dB gain horn antenna (DBG-520) with perfectly conducting electric walls (f = 10 GHz).

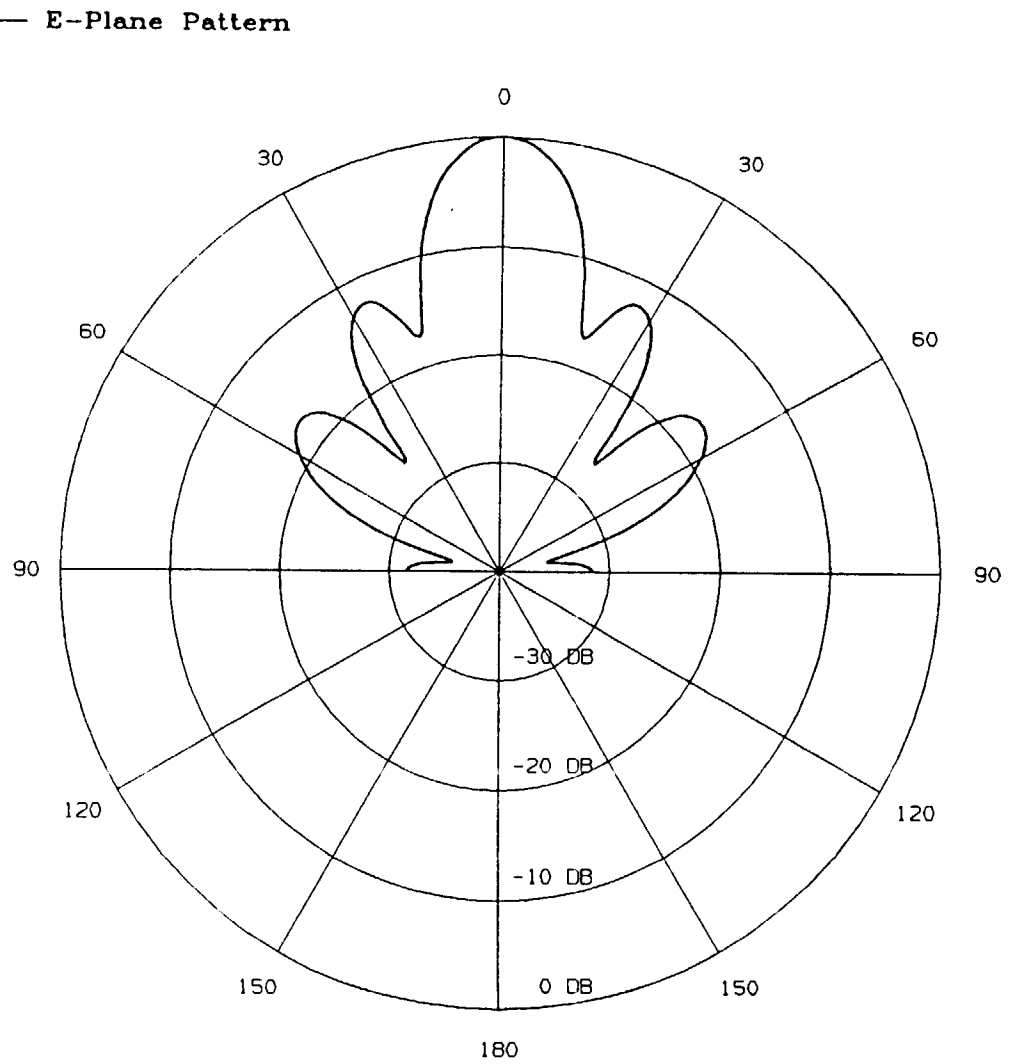

Figure 3. Normalized amplitude pattern for 20dB gain horn antenna (DBG-520) with perfectly conducting electric walls (f = 10 GHz).

good agreements, although the cross polarization has not yet been accounted for.

To investigate the effect of the lossy coating on the radiation pattern, two sets of the lossy materials were used to cover the top and bottom walls of the horn. This is intended to improve the E-plane pattern. The plots shown in Figures 4 and 5 are obtained by uniformly covering the top and bottom walls with a layer of AlSb with a thickness of $0.001\lambda_o$ (3×10^{-5} meters). The material has a relative dielectric constant of 11 and a resistivity of 0.005 $\Omega \cdot m$. The resulting E-plane pattern shows about 2-dB improvement in the sidelobes. Figure 6 and Figure 7 are obtained based on a material which has a relative dielectric constant of 3 and a sheet resistance of 1500 Ω per square. The thickness of this material is 2 mils (5.08×10^{-5} meters). The resulting E-plane pattern shows about 3-dB improvement in the first sidelobe and 4-dB improvement in the second sidelobe.

Further improvement can be expected by increasing the thickness of the coating. However, the validity of our impedance boundary condition becomes questionable. A better impedance condition has been developed; however it has not yet been implemented in the computer program.

In the moment method solution of this project, the computations of the matrix elements are the most tedious part of the work. We have

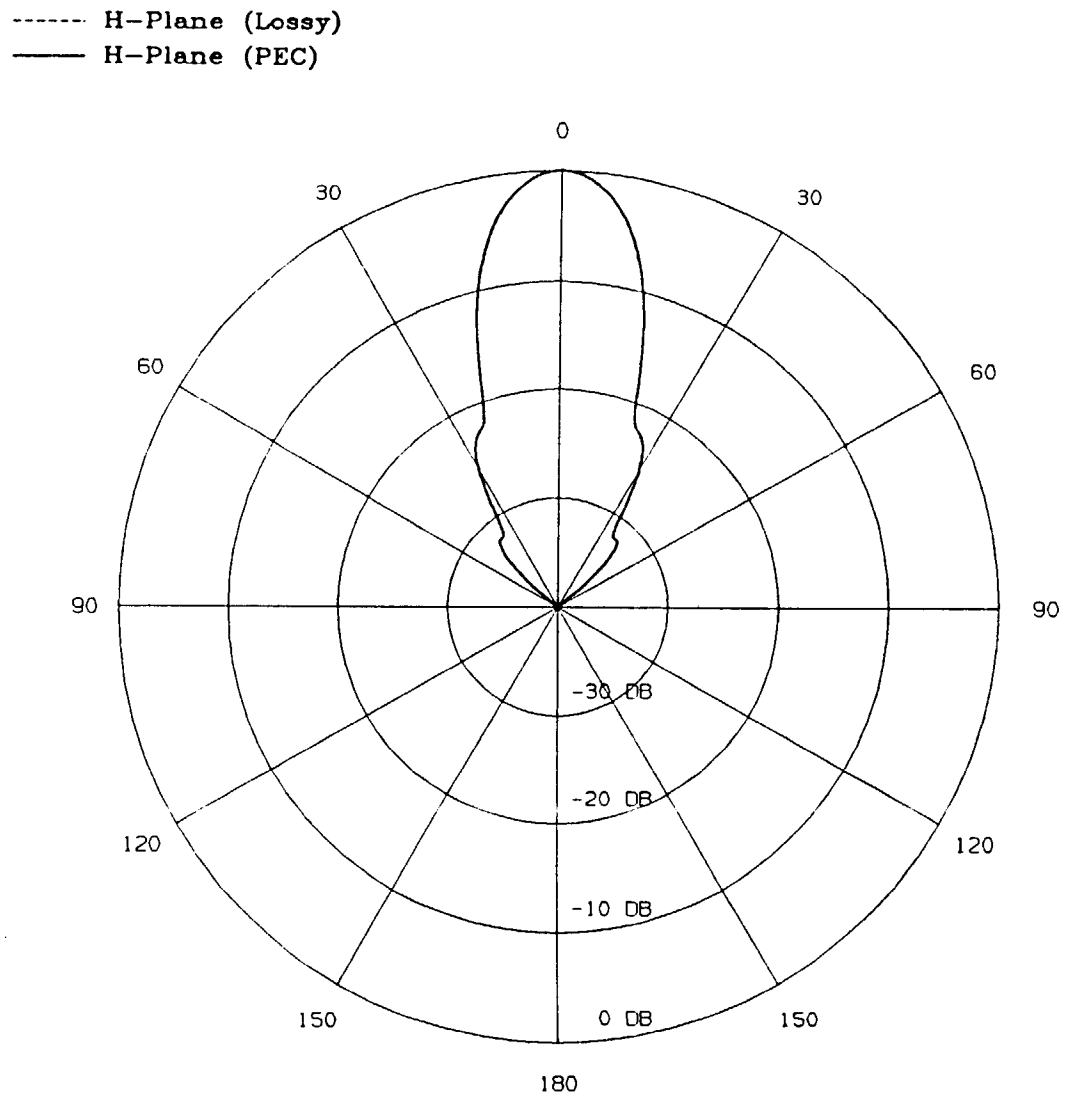

Figure 4. Normalized amplitude pattern for 20dB gain-horn antenna (DBG-520) with upper and lower walls covered with AlSb (f = 10 GHz).

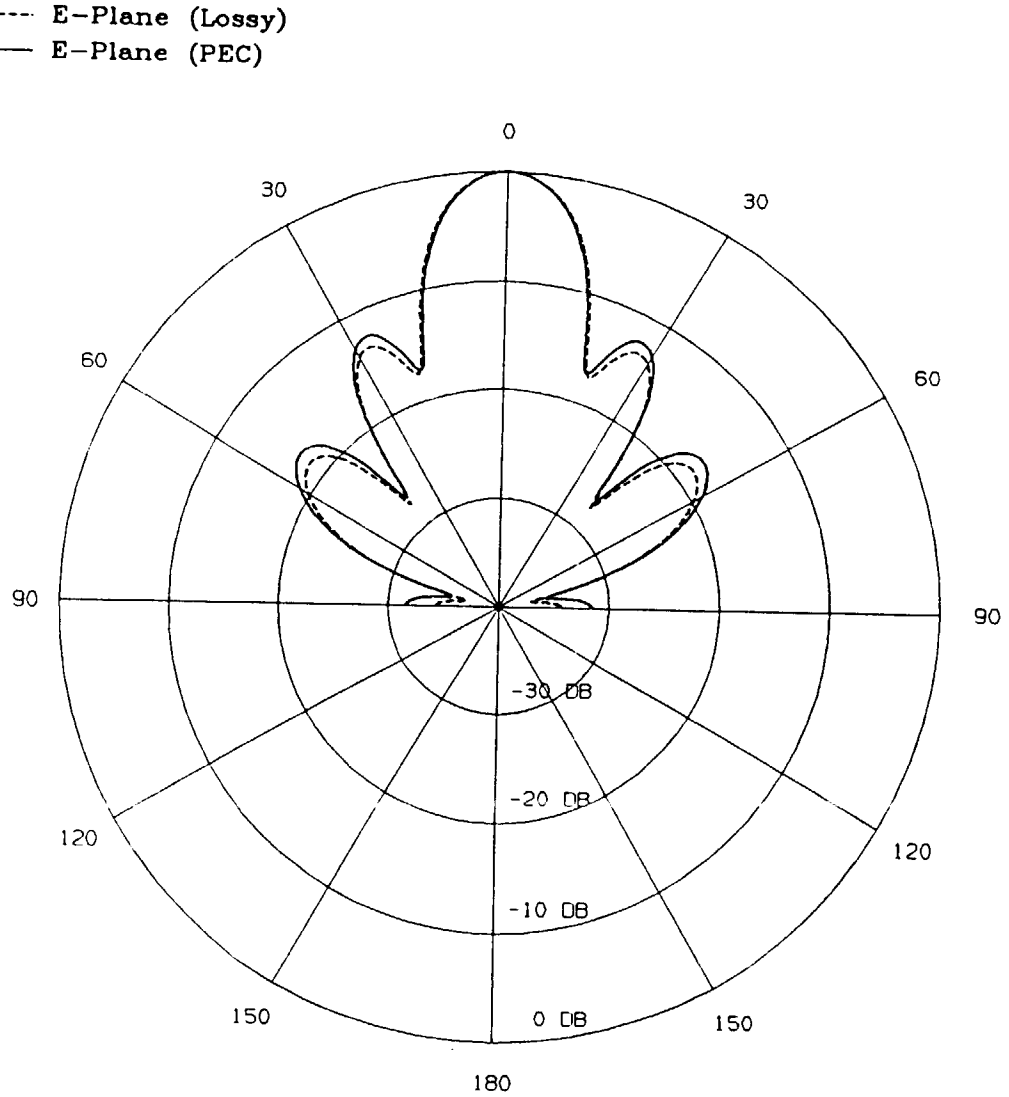

Figure 5. Normalized amplitude pattern for 20dB gain-horn antenna (DBG-520) with upper and lower walls covered with AlSb (f = 10 GHz).

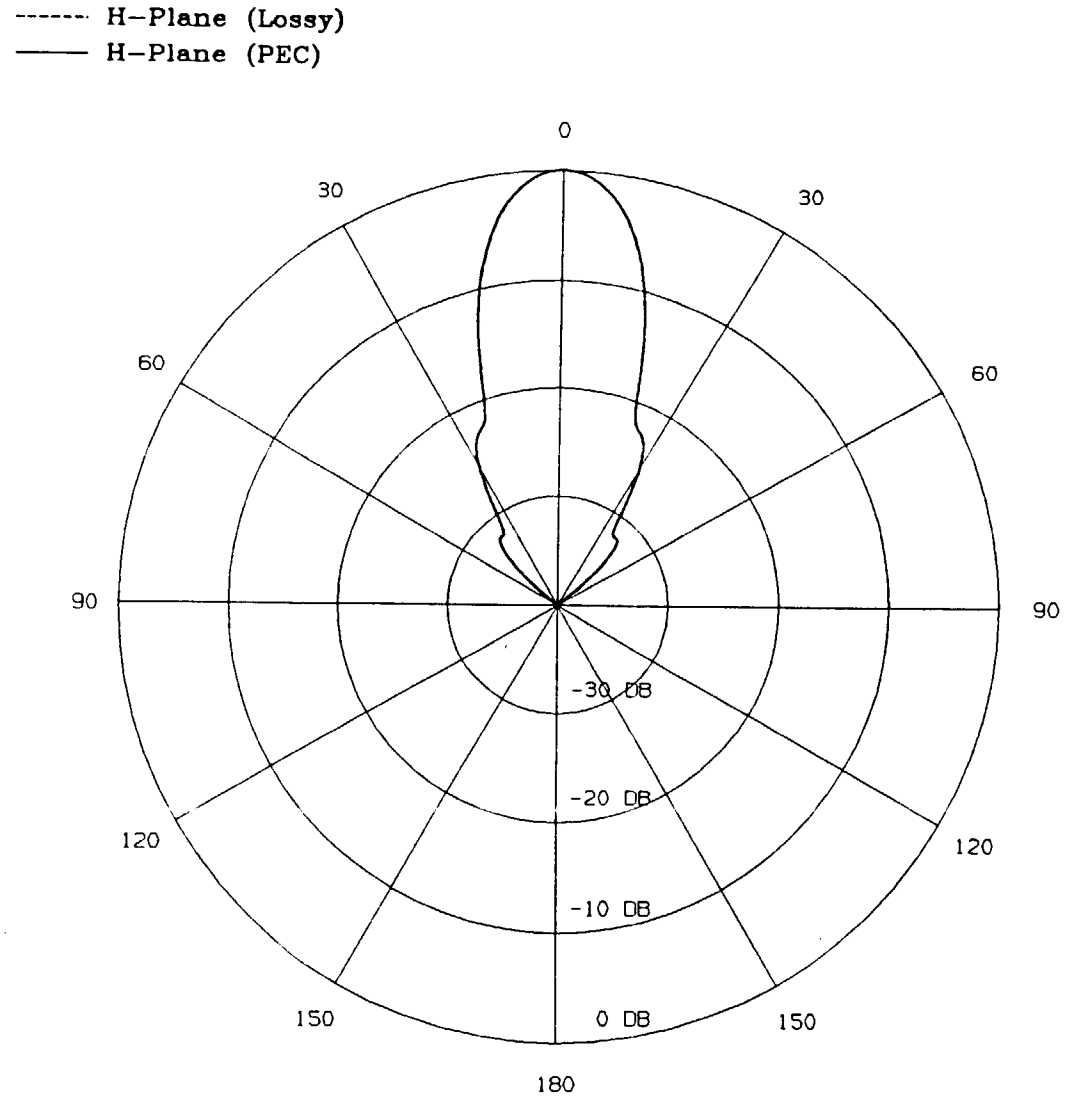

Figure 6. Normalized amplitude pattern for 20dB gain-horn antenna (DBG-520) with upper and lower walls covered with lossy material (f = 10 GHz).

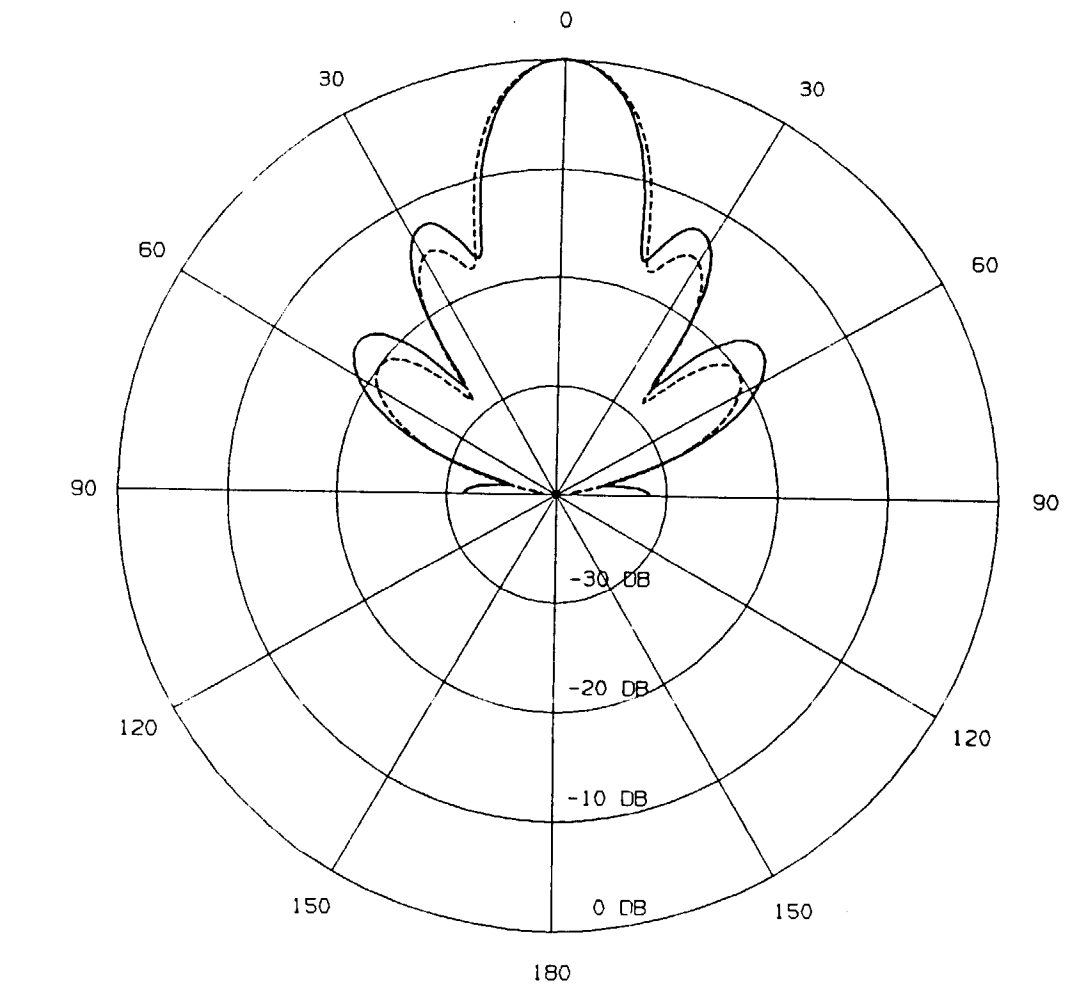

Figure 7. Normalized amplitude pattern for 20dB gain-horn antenna (DBG-520) with upper and lower walls covered with lossy material (f = 10 GHz).

basically fullfilled this task. Although we still did not have time to connect all parts of the work together to realize the synthesis problem, we can say we are progressing well toward that goal.

II. Future Work

Future work will be concentrated on the following items:

1. To include the cross polarization components of the equivalent magnetic currents on the two appertures.
2. To compare this integral equation method with another rigorous method by H. Patzelt and F. Arndt [1].
3 To investigate the realization of the sheet impedance needed to control the radiation pattern, and to extensively verify the validity of the impedance boundary condition.
4. To reassemble the matrix equation to solve the synthesis problem as was presented in the previous report.

REFERENCES

1. Hartmut Patzelt and Fritz Arndt, "Double-plane steps in rectangular waveguide and their application for transformers, Irises, and filters," *IEEE Trans.* Microwave Theory Tech., vol. MTT-30, pp.771-776, May, 1982.